Momentum distributions and short-range correlations in the deuteron and ^{3}He with modern chiral potentials

Laura Elisa Marcucci, Francesca Sammarruca, Michele Viviani, and Ruprecht Machleidt

Phys. Rev. C **99**, 034003 — Published 14 March 2019

DOI: 10.1103/PhysRevC.99.034003

Momentum distributions and short-range correlations in the deuteron and ^{3}He with modern chiral potentials

Laura Elisa Marcucci,[1,2] Francesca Sammarruca,[3] Michele Viviani,[2] and Ruprecht Machleidt[3]

[1] *Dipartimento di Fisica "Enrico Fermi", Università di Pisa, Largo Bruno Pontecorvo 3 - I-56127 Pisa, Italy*
[2] *Istituto Nazionale di Fisica Nucleare, Sezione di Pisa, Largo Bruno Pontecorvo 3 - I-56127 Pisa, Italy*
[3] *Department of Physics, University of Idaho, Moscow, ID 83844, USA*

(Dated: February 3, 2019)

We study momentum distributions and short-range correlation probabilities in A=2 and A=3 systems. First, we show results with phenomenological and meson-theoretic two- and three-nucleon forces to verify consistency with previous similar studies. We then apply most recent high-quality chiral nucleon-nucleon potentials up to fifth order in the chiral expansion together with the leading chiral three-nucleon force. The focal points of our investigations are the model dependences of one- and two-body momentum distributions and the impact of three-body forces on them.

I. INTRODUCTION

The study of high-momentum distributions in nuclei is fundamentally important as it can reveal information about the short-range few-nucleon dynamics when the few-nucleon system under consideration is surrounded by the medium. In this work, we focus on short-range correlation (SRC) in the deuteron and, with particular emphasis, in ^{3}He.

The lively discussion recently stimulated by inclusive electron scattering measurements at high momentum transfer on both light and heavy nuclei provides additional motivation for studying SRCs. In fact, those measurements have been analyzed with the purpose of extracting information on SRCs [1–5]. In a suitable range of Q^2 (the four-momentum squared of the virtual photon) and of x_B (the Bjorken variable), the cross section for the $A(e,e')X$ process is factorized such that cross section ratios for nuclei A_1 and A_2 can be related to the respective probability of a nucleon to be involved in (either two-body or three-body) SRCs [1]. When extended to nuclear matter, this probability is equivalent to the "wound integral", which measures the amount of correlations in the wave function and the G-matrix [6]. We recall, in passing, that the wound integral is the integral of the amplitude squared of the "defect function", defined as the difference between the correlated and the uncorrelated wave functions.

Information about two-body SRCs can also be obtained in coincidence experiments involving knock-out of a nucleon pair with protons [7] or electrons [8–11].

The plateaus seen in the ratios of inclusive scattering cross section [1, 2] can be attributed to the dominance of SRCs for momenta above approximately 2 fm^{-1}. That is, when the electron scatters from a high-momentum nucleon in the nucleus, the scattering can be viewed as an electron-deuteron interaction, with the other $A-2$ nucleons essentially at rest. More specifically, in an appropriate range of Q^2 and x_B, the ratio

$$R(A_1,A_2) = \frac{\sigma(A_1,Q^2,x_B)/A_1}{\sigma(A_2,Q^2,x_B)/A_2} \tag{1}$$

is expected to display scaling behavior. Under those circumstances, the cross section ratio can be expressed as

$$\frac{\sigma(A_1,Q^2,x_B)}{\sigma(A_2,Q^2,x_B)} = \frac{A_1}{A_2} R(A_1,A_2)\ , \tag{2}$$

where R is identified with the ratio of SRC probabilities in the two nuclei A_1 and A_2. Therefore, measurements of inclusive electron scattering cross section ratios in the appropriate kinematical region can be related to the ratio of SRC probabilities, and ultimately the absolute probability for a particular nucleus, given a suitable starting point, which, quite naturally, one would take to be the deuteron.

Deuteron momentum distributions in the context of SRCs were studied in Ref. [12] using local and non-local realistic two-nucleon (2N) interactions. Those included: purely phenomenological local potentials, such as the Argonne v_{18} [13] (AV18) or the Nijmegen II [14] models, non-local meson-theoretic models, such as the charge dependent Bonn (CDBonn) potential [15], and state-of-the-art non-local chiral potentials [16–18]. In the study of Ref. [12], it was concluded that predictions of high-momentum distributions in the deuteron with non-local meson-exchange forces *or* state-of-the-art chiral forces are systematically lower than those obtained with the local AV18 or Nijmegen II potentials.

The analysis of Ref. [12] highlights non-localities in the tensor force as the source of differences in SRC among the various predictions. At this point, it is appropriate to recall that the presence of non-locality in the tensor force has

been found since a long time to be a desirable feature in nuclear structure calculations. (For a discussion on the impact of non-locality in the one-pion exchange, see, for instance, Refs. [19–21].)

This paper contains updates and major extensions of the work of Ref. [12], presenting a simultaneous study of momentum distributions in the deuteron and in ^{3}He. First, we calculate the deuteron momentum distribution using the most recent chiral 2N potentials from Ref. [22], from leading to fifth chiral order. These interactions are better and more consistent than the ones of Refs. [16–18] used in Ref. [12], because the same power counting scheme and cutoff procedures are used at each order. In addition, the πN low-energy constants (LECs) are the very accurate ones determined in the Roy-Steiner analysis of Ref. [23]. The uncertainty associated with these LECs is sufficiently small that variations within their errors have negligible impact on the construction of the potentials, which are non-local and of soft nature. A point worth mentioning is that these 2N forces can predict a triton binding energy around 8.1 MeV, leaving only very small room for three-nucleon (3N) forces.

We then proceed to consider the single-nucleon (1N) and 2N momentum distributions in ^{3}He using the phenomenological AV18 and the meson-theoretic CDBonn potentials, alone or augmented by 3N forces, namely the Urbana IX (UIX) model [24] in conjunction with AV18, and the Tucson-Melbourne (TM) [25] 3N force in conjunction with CDBonn. This will allow us to quantify the 3N force contributions within the framework of these older forces. To verify our calculations, results obtained with the AV18 and AV18/UIX potential models will be compared with the previous studies of Refs. [26–28].

Having established a reliable baseline, we shift our focus to the more novel aspects of this work, namely the most recent high precision chiral 2N potentials [22] and corresponding chiral 3N force. The main motivation behind this calculation can be explained as follows. The presence of high-momentum components in the nuclear wave function is an indication of SRCs. At the two-body level, SRCs originate from the (repulsive) short-range central and tensor force, which, in the well-established and still popular meson-exchange phenomenology, are described by ω- and ρ-meson exchange, respectively. Although realistic meson-theoretic or purely phenomenological interactions are frequently employed in contemporary calculations of nuclear structure and reactions, this approach has some intrinsic problems/limitations. First, the connection between the 2N and the applied 3N force does not rest on firm grounds. Second, no clear mechanism exists to quantify and control the theoretical uncertainty of a prediction. These problems can be addressed systematically in the chiral effective field theory (χEFT) approach, which, in principle, provides a well-defined prescription to develop nuclear forces in an internally consistent manner at each order of a systematic perturbative expansion. In fact, using effective degrees of freedom, namely hadrons (nucleons and pions), and maintaining a link with quantum chromodynamics (QCD) through the symmetries of low-energy QCD, χEFT has become a well-established and, in principle, model-independent framework to develop nuclear forces and quantify the theoretical uncertainty at each order of the expansion. Therefore, we find it both important and insightful to perform these calculations using state-of-the-art chiral interactions.

The paper is organized as follows: In Sec. II we set the stage with a brief discussion on the deuteron, while we address ^{3}He in Sec. III. In the latter section, we will first present a brief review of the numerical techniques used to calculate the $A = 3$ nuclear wave functions and the 1N and 2N momentum distributions. Then we will show and discuss results obtained with the older AV18 and CDBonn potential models, augmented or not by the UIX [24] and the TM [25] 3N force, respectively, as well as the chiral 2N potentials of Ref. [22], without or with the chiral 3N force. We will also discuss the procedure adopted to determine the two LECs entering the leading 3N force. Our conclusions and future plans are summarized in Sec. IV.

II. HIGH-MOMENTUM DISTRIBUTION AND SHORT-RANGE CORRELATIONS IN THE DEUTERON

To best put this study in context, we begin with a quick review of the 2N bound state. In particular, we present in Fig. 1 the deuteron momentum distributions $\rho(k)$, defined as the Fourier transform squared of the coordinate-space deuteron wave function. On the left side of the figure, we show the results, with focus on high-momentum components, obtained with the latest chiral interactions of Ref. [22] from leading to fifth order (N^{4}LO). On the right side of the figure, we show for comparison the same quantities calculated as in Ref. [12] with the older chiral potentials of Refs. [16–18]. From inspection of the figure, we can conclude that the convergence pattern has definitely improved with the new potentials.

We then define the probability of SRCs in the deuteron as in Ref. [12], i.e.

$$a_{2N}(d) = 4\pi \int_{k_{min}}^{\infty} \rho(k) k^2 \, dk \, , \tag{3}$$

where k_{min} is taken to be 1.4 fm^{-1} (276 MeV). This definition was adopted in Ref. [1], where the choice of the lower integration limit was suggested by the onset of scaling of the cross section, which should signal the dominance of

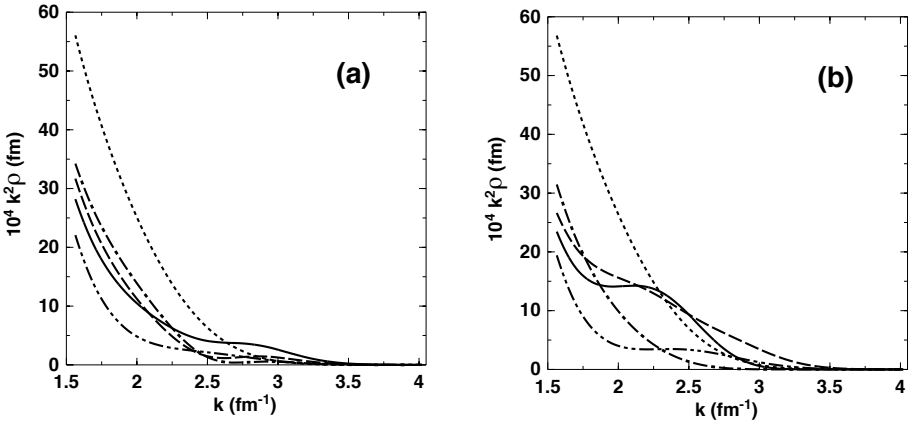

FIG. 1: Panel (a): Momentum distributions in the deuteron predicted with the chiral potentials of Ref. [22] at LO (dotted), NLO (dash-double dot), N^{2}LO (dash-dot), N^{3}LO (dash), N^{4}LO (solid). The cutoff is fixed at $\Lambda = 500$ MeV. Panel (b): Predictions taken from Ref. [12], and are obtained using the chiral potentials of Refs. [16–18].

TABLE I: Probabilities of SRCs as defined in Eq. (3) and deuteron D-state percentage for the chiral interactions considered in panel (a) of Fig. 1. The values in parenthesis, given for comparison, are taken from Ref. [12] and correspond to the distributions shown in panel (b) of Fig. 1. The cutoff Λ is equal to 500 MeV in all cases.

Model	$a_{2N}(d)$	P_D
LO	0.046 (0.047)	0.0729 (0.0757)
NLO	0.015 (0.015)	0.0340 (0.0313)
N^{2}LO	0.026 (0.022)	0.0449 (0.0417)
N^{3}LO	0.024 (0.030)	0.0415 (0.0451)
N^{4}LO	0.024 (0.026)	0.0410 (0.0414)

scattering from a strongly correlated nucleon. In view of Eqs. (1)–(2), the absolute per-nucleon SRC probability in a nucleus A can be deduced if the absolute per-nucleon probability in ^{3}He and the deuteron are calculated or estimated. More precisely,

$$a_{2N}(A) = a_2(A/^3\mathrm{He})a_{2N}(^3\mathrm{He}) \quad \text{and} \quad a_{2N}(^3\mathrm{He}) = a_2(^3\mathrm{He}/d)a_{2N}(d)\ , \tag{4}$$

where $a_2(A_1/A_2)$ is the SRC probability for nucleus A_1 relative to nucleus A_2. The probability in the deuteron was taken to be equal to 0.041 ± 0.008 in Ref. [2]. We list in Table I the integrated probabilities $a_{2N}(d)$ defined in Eq. (3), calculated integrating the curves of Fig. 1 (panel (a)). As an additional, related information, we also show the corresponding D-state percentage. In fact, deuteron D-state probabilities are larger with stronger short-range central and tensor components of the nuclear force which, for the non-local chiral interactions and, generally, for non-local interactions, are softer than for the local AV18 potential. The values in parenthesis correspond to the distributions displayed on the right of Fig. 1, i.e. obtained with the older chiral potentials of Refs. [16–18]. As the table shows, there are huge variations between the LO and the NLO cases, and still large differences between NLO and N^{2}LO. Variations at higher orders indicate a clear convergence pattern, definitely improved by the use of the newest potentials. Finally we notice that the deuteron integrated probabilities $a_{2N}(d)$ display significant model-dependence, as the corresponding values obtained with the AV18 and the CDBonn potentials are 0.042 and 0.032, respectively. We will show below that similar considerations apply to ^{3}He as well.

III. HIGH-MOMENTUM DISTRIBUTION AND SHORT-RANGE CORRELATIONS IN THE ^3He NUCLEUS

A. Theoretical formalism

We briefly review the method used to solve the $A = 3$ quantum mechanical problem, i.e. the Hyperspherical Harmonics (HH) method. This method has the great advantage that we can work both in coordinate- and momentum-space, with no restriction on the choice of the nuclear potential model, either local or non-local. The starting point are the so-called Jacobi coordinates, which are defined in coordinate-space as [29, 30]

$$\begin{aligned} \mathbf{x}_p &= \frac{1}{\sqrt{2}}(\mathbf{r}_j - \mathbf{r}_i) \ , \\ \mathbf{y}_p &= \sqrt{\frac{2}{3}}\left(\mathbf{r}_k - \frac{1}{2}(\mathbf{r}_i + \mathbf{r}_j)\right) \ , \end{aligned} \tag{5}$$

where p represents an even permutation of $i, j, k = 1, 2, 3$, with $p = 1$ for $i, j, k = 2, 3, 1$, and $\mathbf{r}_i$ is the position of the i-th particle. The conjugate Jacobi momenta (in unit of $\hbar = 1$) are defined as

$$\begin{aligned} \mathbf{q}_p &= \frac{1}{\sqrt{2}}(\mathbf{p}_j - \mathbf{p}_i) \ , \\ \mathbf{k}_p &= \sqrt{\frac{2}{3}}\left(\mathbf{p}_k - \frac{1}{2}(\mathbf{p}_i + \mathbf{p}_j)\right) \ , \end{aligned} \tag{6}$$

$\mathbf{p}_i$ being the momentum of the i-th particle. The next step is to introduce the so-called hyperradius ρ and hypermomentum Q as

$$\begin{aligned} \rho &= \sqrt{\mathbf{x}_p^2 + \mathbf{y}_p^2} \ , \\ Q &= \sqrt{\mathbf{k}_p^2 + \mathbf{q}_p^2} \ , \end{aligned} \tag{7}$$

and the hyperangle $\phi_p^{(\rho/Q)}$, given by

$$\begin{aligned} \tan\phi_p^{(\rho)} &= \frac{y_p}{x_p} \ , \\ \tan\phi_p^{(Q)} &= \frac{k_p}{q_p} \ . \end{aligned} \tag{8}$$

We note that ρ and Q do not depend on the considered permutation, while $\phi_p^{(\rho)}$ or $\phi_p^{(Q)}$ do. Then, the HH functions for the $A = 3$ system are given in coordinate space by

$$\mathcal{Y}_{\alpha,n}(\Omega_p^{(\rho)}) = [[Y_l(\hat{\mathbf{x}}_p) \otimes Y_L(\hat{\mathbf{y}}_p)]_{\Lambda\Lambda_z} \otimes [\chi_{S_{ij}} \otimes \frac{1}{2}]_{\Sigma\Sigma_z}]_{JJ_z} [\eta_{T_{ij}} \otimes \frac{1}{2}]_{TT_z} P_{n,l,L}(\phi_p^{(\rho)}) \ , \tag{9}$$

where $\Omega_p^{(\rho)} = (\phi_p^{(\rho)}, \hat{\mathbf{x}}_p, \hat{\mathbf{y}}_p)$ and

$$P_{n,l,L}(\phi_p^{(\rho)}) = N_{n,l,L}(\cos\phi_p^{(\rho)})^l (\sin\phi_p^{(\rho)})^L P_n^{L+1/2,l+1/2}(\cos 2\phi_p^{(\rho)}) \ , \tag{10}$$

$N_{n,l,L}$ being a normalization coefficient and $P_n^{L+1/2,l+1/2}(\cos 2\phi_p^{(\rho)})$ a Jacobi polynomial of degree n. In Eq. (9), $Y_l(\hat{\mathbf{x}}_p)$ and $Y_L(\hat{\mathbf{y}}_p)$ are spherical harmonics in the two Jacobi coordinates, coupled to the total orbital angular momentum Λ, Λ_z, $\chi_{S_{ij}}$ ($\eta_{T_{ij}}$) is the spin (isospin) function of the pair ij, where the spins (isospins) of the particles i and j are coupled to S_{ij} (T_{ij}), which is itself coupled to the spin (isospin) 1/2 of particle k to give the total spin (isospin) Σ, Σ_z (T, T_z). The total orbital angular momentum Λ and the total spin Σ are coupled to the total angular momentum J, J_z. Finally, we remark that the grand-angular momentum is defined as $G = 2n + l + L$, and we have labelled with the channel index α the set of quantum numbers $[l, L, \Lambda, S_{ij}, \Sigma, T_{ij}, T]$ which determine the spin-isospin-angular state. An expression similar to Eq. (9) holds in momentum-space, with appropriate changes.

Having introduced the HH functions, the $A = 3$ nuclear wave function can be written as

$$\Psi = \sum_{\alpha,n} u_{\alpha,n}(\rho) \sum_p \mathcal{Y}_{\alpha,n}(\Omega_p^{(\rho)}) \ , \tag{11}$$

where $u_{\alpha,n}(\rho)$ is the hyperradial function to be determined. Similarly, in momentum-space we can write

$$\Psi = \sum_{\alpha,n} w_{\alpha,n}(Q) \sum_{p} \mathcal{Y}_{\alpha,n}(\Omega_p^{(Q)}) \ , \tag{12}$$

where $w_{\alpha,n}(Q)$ is the function of the hypermomentum Q, and it is related to $u_{\alpha,n}(\rho)$ via essentially a Fourier transform [29], i.e.

$$w_{\alpha,n}(Q) = (-i)^G \int_0^\infty d\rho \, \frac{\rho^5}{Q\rho^2} \, \mathcal{J}_{G+2}(Q\rho) u_{\alpha,n}(\rho) \ , \tag{13}$$

where $\mathcal{J}_{G+2}(Q\rho)$ is a Bessel function. Finally, the functions $u_{\alpha,n}(\rho)$ (or $w_{\alpha,n}(Q)$) are themselves expanded on a basis of Laguerre polynomials (or their Fourier transform) as

$$u_{\alpha,n}(\rho) \ = \ \sum_k c_{\alpha,n,k} \ {}^{(5)}L_k(\gamma\rho) \, \mathrm{e}^{-\gamma\rho/2} \ , \tag{14}$$

where $c_{\alpha,n,k}$ are unknown coefficients and γ is a non-linear parameter, chosen to be 4 fm^{-1} for the local AV18 or AV18/UIX potentials, and 7 fm^{-1} for the other non-local potentials. These values are the ones used in Refs. [29, 30]. Equations (11)–(14) can be cast in a compact form as

$$\Psi = \sum_\mu c_\mu \phi_\mu \ , \tag{15}$$

where ϕ_μ are given either in coordinate- or momentum-space. What is essential is that the c_μ coefficients of the expansion are the same in both cases. These coefficients are determined using the Rayleigh-Ritz variational principle, and the problem of determining c_μ and the energy E is reduced to a generalized eigenvalue problem,

$$\sum_{\mu'} c_{\mu'} \langle \phi_\mu | H - E | \phi_{\mu'} \rangle = 0 \ . \tag{16}$$

The advantage of having ϕ_μ expressed either in coordinate- or in momentum-space is clear: the matrix elements of local operators will be calculated in coordinate-space, those of non-local operators in momentum-space. Furthermore, the 1N and 2N momentum-distributions can be written straightforward in momentum-space, without the need to perform any additional Fourier transform, unlike what was done in Refs. [26–28]. We will define and evaluate these momentum-distributions in the next sections.

We conclude this section by discussing the construction of the 3N force in the chiral approach. As is well known, the chiral 3N force appears for the first time at N2LO. It consists of three contributions: the two-pion exchange (2PE) term, the one-pion exchange (1PE) diagram, and a short-range contact term. These contributions are shown in Fig. 2. All the three diagrams are multiplied by LECs. In particular, the 2PE term depends on the LECs $c_{1,3,4}$, which are

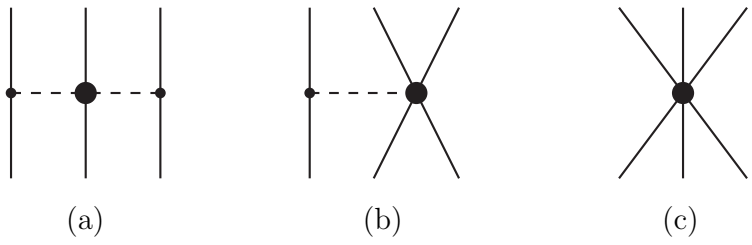

FIG. 2: The three contributions to the 3N force at N2LO. Panel (a) and (b) correspond to the 2PE and 1PE terms, respectively, while panel (c) corresponds to the contact contribution.

already present in the 2PE part of the 2N force, and therefore they are already fixed. Instead, the 1PE and the contact terms are multiplied by two new LECs, c_D and c_E, respectively. We determine them within a well established procedure (see Ref. [31] and references therein), repeated in Ref. [32] for the new chiral potentials of Ref. [22]. The LECs c_D and c_E are essentially constrained to reproduce the $A = 3$ binding energies and the Gamow-Teller (GT) matrix element of tritium β-decay. For completeness, the values of c_D and c_E from Table I and II of Ref. [32] are reported again here in Table II and III, which include, in addition, the values obtained with $\Lambda = 550$ MeV. In the

TABLE II: Values for the LECs $c_{1,3,4}$, c_D and c_E at the chiral orders N2LO, N3LO and N4LO. The c_D and c_E LECs reproduce the $A = 3$ binding energies and the GT matrix element in tritium β-decay, as explained in the text. The 2PE N3LO 3N interactions are not included, i.e. the $c_{1,3,4}$ LECs in the 3N force are those of Table II of Ref. [22]. The numbers in parentheses indicate the error arising from the fitting procedure.

	Λ (MeV)	c_1	c_3	c_4	c_D	c_E
N2LO	450	–0.74	–3.61	2.44	0.935(0.215)	0.12(0.04)
	500	–0.74	–3.61	2.44	0.495(0.195)	–0.07(0.04)
	550	–0.74	–3.61	2.44	–0.140(0.190)	–0.44(0.03)
N3LO	450	–1.07	–5.32	3.56	0.675(0.205)	0.31(0.05)
	500	–1.07	–5.32	3.56	–0.945(0.215)	–0.68(0.04)
	550	–1.07	–5.32	3.56	–1.610(0.220)	–1.69(0.03)
N4LO	450	–1.10	–5.54	4.17	1.245(0.225)	0.28(0.05)
	500	–1.10	–5.54	4.17	–0.670(0.230)	–0.83(0.03)
	550	–1.10	–5.54	4.17	–1.245(0.175)	–1.91(0.02)

TABLE III: Same as Table II but including the 2PE 3N interaction at N3LO and N4LO, i.e. the $c_{1,3,4}$ LECs in the 3N force are those of Table IX of Ref. [22].

	Λ (MeV)	c_1	c_3	c_4	c_D	c_E
N2LO	450	–0.74	–3.61	2.44	0.935(0.215)	0.12(0.04)
	500	–0.74	–3.61	2.44	0.495(0.195)	–0.07(0.04)
	550	–0.74	–3.61	2.44	–0.140(0.190)	–0.44(0.03)
N3LO	450	–1.20	–4.43	2.67	0.670(0.210)	0.41(0.05)
	500	–1.20	–4.43	2.67	–0.750(0.210)	–0.41(0.04)
	550	–1.20	–4.43	2.67	–1.350(0.200)	–1.14(0.03)
N4LO	450	–0.73	–3.38	1.69	0.560(0.220)	0.46(0.05)
	500	–0.73	–3.38	1.69	–0.745(0.225)	–0.15(0.04)
	550	–0.73	–3.38	1.69	–1.030(0.200)	–0.57(0.02)

first table, the c_D and c_E values are obtained using the 3N force up to N2LO. The complete 3N force beyond N2LO is very complex and often neglected in nuclear structure studies. However, the 2PE component of the 3N force can be calculated fully up to N4LO. In Ref. [33] it was shown that the 2PE 3N force has essentially the same analytical structure at N2LO, N3LO, and N4LO. Thus, one can add the three orders of this 3N force component and parametrize the result in terms of effective LECs. These effective LECs are taken from Table IX of Ref. [22] and shown here in Table III. By using these $c_{1,3,4}$ in the mathematical expression of the N2LO 3N force, one can include the 2PE parts of the 3N force up to N3LO and N4LO in a simple way. Obviously, the LECs c_D and c_E are fitted again for each case and are listed in Table III. The error arising from the fitting procedure, shown in parentheses, is quite large. On the other hand, we have observed that the impact of the 3N interaction on the momentum distributions and SRCs is weak (see below). Thus, we find it appropriate to use in our study the wave functions obtained adopting the central values of c_D and c_E.

Some comments are in place concerning the chosen range for the cutoff, Λ, between 450 and 550 MeV. On the one hand, we wish to stay below the breakdown scale, which, as discussed in Ref. [34], is expected to be around 600 MeV. On the other hand, softer cutoffs impact the ability to describe 2N scattering up to moderate energies (about 300 MeV in terms of laboratory energy), which motivates our lower limit.

B. Single-nucleon momentum distributions and corresponding integrated short-range correlations probabilities

The 1N momentum distributions for a particular nucleon (p or n) with momentum $\mathbf{k}$ in ^{3}He are defined as

$$n^p(k) \;=\; \frac{1}{2}\int d\hat{\mathbf{k}}\; d\mathbf{q}\; \Psi^\dagger(\mathbf{k},\mathbf{q}) P_p \Psi(\mathbf{k},\mathbf{q}) \;,$$

$$n^n(k) \;=\; \int d\hat{\mathbf{k}}\, d\mathbf{q}\, \Psi^\dagger(\mathbf{k},\mathbf{q}) P_n \Psi(\mathbf{k},\mathbf{q}) \;, \tag{17}$$

where we have fixed the permutation to be $p = 1$, i.e. the particular nucleon is fixed to be particle 1, and therefore $\mathbf{k} = \mathbf{k}_{p=1}$ and $\mathbf{q} = \mathbf{q}_{p=1}$, in the notation of Eq. (6). Furthermore, $P_{p/n}$ is the proton/neutron projection operator acting on particle 1. With this definition, the 1N momentum distributions are normalized as

$$4\pi \int k^2\, dk\, n^{n/p}(k) = 1 \;. \tag{18}$$

We have verified that Eqs. (17) and (18) are consistent with those of Ref. [26].

We have first calculated the 1N momentum distributions using the AV18 [13] or CDBonn [15] phenomenological potentials, with and without the 3N force (UIX [24] or TM [25] for AV18 or CDBonn, respectively). The results are shown in Fig. 3. From those, we conclude that 3N force contributions are small, and only noticeable for $k \geq 2$ fm^{-1}. On the contrary, potential-model dependence is large in the range $k \geq 2$ fm^{-1}, an aspect which will be a recurrent theme throughout this paper. Furthermore, some small model dependence is present also in the low k region, for $k \leq 0.5$ fm^{-1}, at the level of 1%. Only the results at $k = 0$ fm^{-1} differ at the 3% level. This suggests the presence of correspondigly small differences in the asymptotic part of the wave functions. Note that, in order to avoid an excessively cumbersome presentation, results from Ref. [26] and Ref. [28], obtained using AV18 HH and AV18/UIX Variational Monte Carlo (VMC) wave functions, are not shown. However, we have verified that we are in agreement with Refs. [26, 28], with small differences only in the high-k tail of the distributions. Comparison between our results and those of Refs. [26–28] will be shown in the case of the back-to-back 2N momentum distribution (see below).

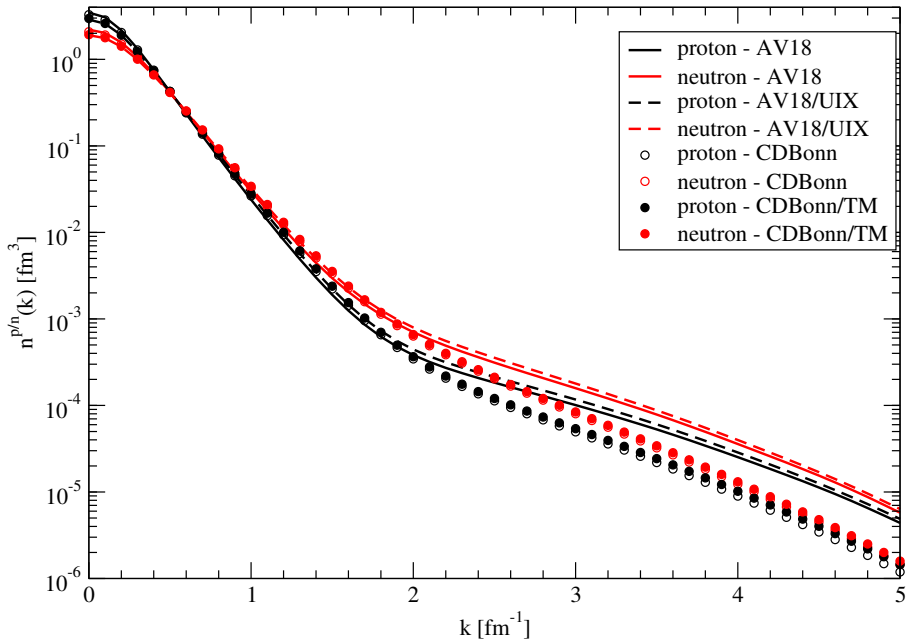

FIG. 3: (Color online) The 1N momentum distributions $n^{p/n}(k)$, calculated using the AV18 and CDBonn 2N interaction, AV18/UIX and CDBonn/TM 2N and 3N interaction models.

We then move to study the 1N momentum distributions using chiral potentials [22]. In Figs. 4 and 5 we present the neutron and proton 1N momentum distribution obtained with only 2N forces at LO, NLO, N2LO, N3LO and N4LO in panel (a), and adding the 3N force, with LECs from Table II (model I) or III (model II). These 1N momentum distributions are calculated with cutoff value fixed at $\Lambda = 500$ MeV. The figure shows that, for small values of k, all predictions at NLO and higher orders are quite similar. Overall, differences between the N3LO and N4LO curves are small enough to suggest a reasonable convergence pattern. The 3N force contributions are found again to be very small, and therefore the differences between the predictions from model I and model II for the 3N force are even smaller.

The 1N momentum distributions $n^n(k)$ and $n^p(k)$ calculated with and without 3N interaction, at different chiral orders and for different values of the cutoff Λ, are shown in Figs. 6 and 7, respectively. By inspection of the figures, we can see that cutoff dependence appears comparable at all orders. Naturally, sensitivity is more pronounced in the high k_{rel} region, where larger values of the cutoff produce "harder" distributions.

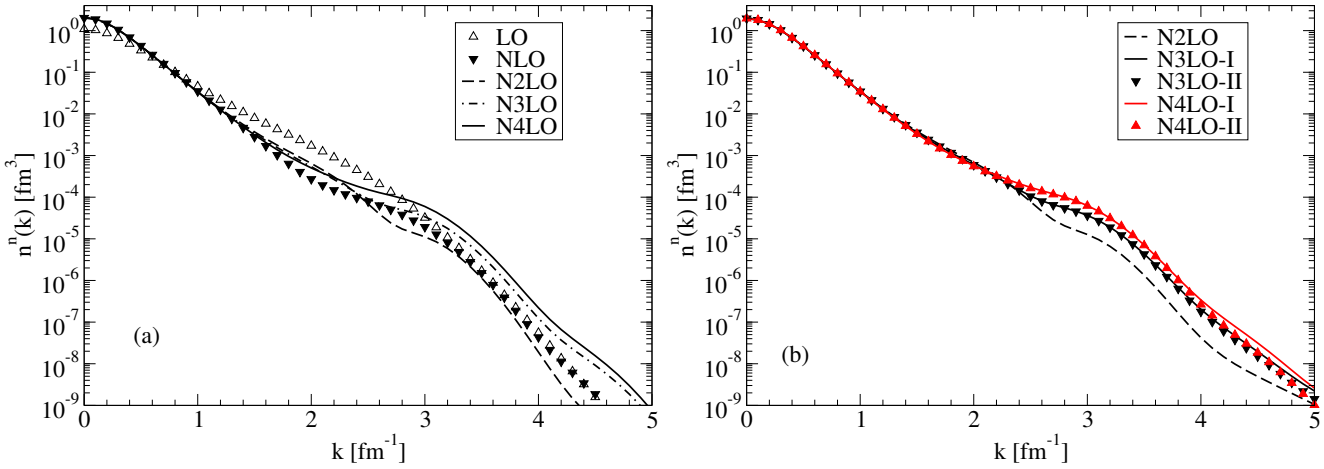

FIG. 4: (Color online) The neutron momentum distributions $n^n(k)$, calculated using only 2N (panel (a)) and 2N+3N (panel (b)) chiral interactions, with $\Lambda = 500$ MeV. The different chiral order are labelled as in the text. In particular, in panel (b), we have indicated with "I" and "II" the results obtained using the LECs of Table II and III, respectively.

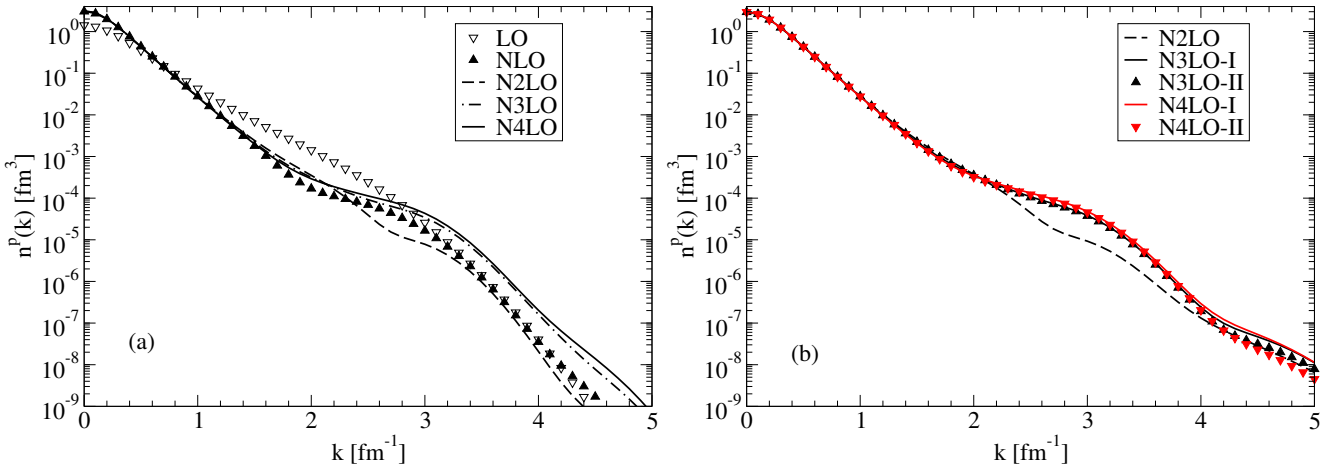

FIG. 5: Same as Fig. 4 but for the proton momentum distributions $n^p(k)$. To be noticed that in panel (b) the N3LO and N4LO results can barely be distinguished.

Finally we consider the integrated probabilities, defined as

$$\mathcal{P}^{p/n}(k_{min}) = 4\pi \int_{k_{min}}^{\infty} n^{p/n}(k)\, k^2\, dk \tag{19}$$

as in Table II of Ref. [26]. The results obtained with the 2N and 2N+3N phenomenological potentials are listed in Table IV. Those obtained using the chiral potentials are presented in Table V. In both tables, we have first calculated $\mathcal{P}^{p/n}(k_{min} = 0)$, in order to verify that the 1N momentum distributions are properly normalized. Note that in our integration, the upper limit of the integral is in fact 5 fm^{-1}. Therefore, the difference of $\mathcal{P}^{p/n}(k_{min} = 0)$ from unity (see Eq. (18)) gives an indication of the importance of the tail of the momentum distribution. By inspection of the tables we can see that $\mathcal{P}^{p/n}(k_{min} = 0) \simeq 1$ within 0.2–0.3%. A comparison of the results of Table IV and V shows again a remarkable model dependence. The results of Table V show also a satisfactory order-by-order convergence.

A glance at Figs. 3 – 7, reveals characteristic differences between the qualitative features of the chiral predictions as compared to the phenomenological and meson-theoretic ones. This is due to the polynomial structure of the (short-range) contact terms used in the construction of the chiral potentials, combined with the exponential regulator function

$$f(p', p) = \exp[-(p'/\Lambda)^{2n} - (p/\Lambda)^{2n}] \,. \tag{20}$$

In the meson-theoretic potentials, the short range is described by heavy-meson exchanges represented by Yukawa

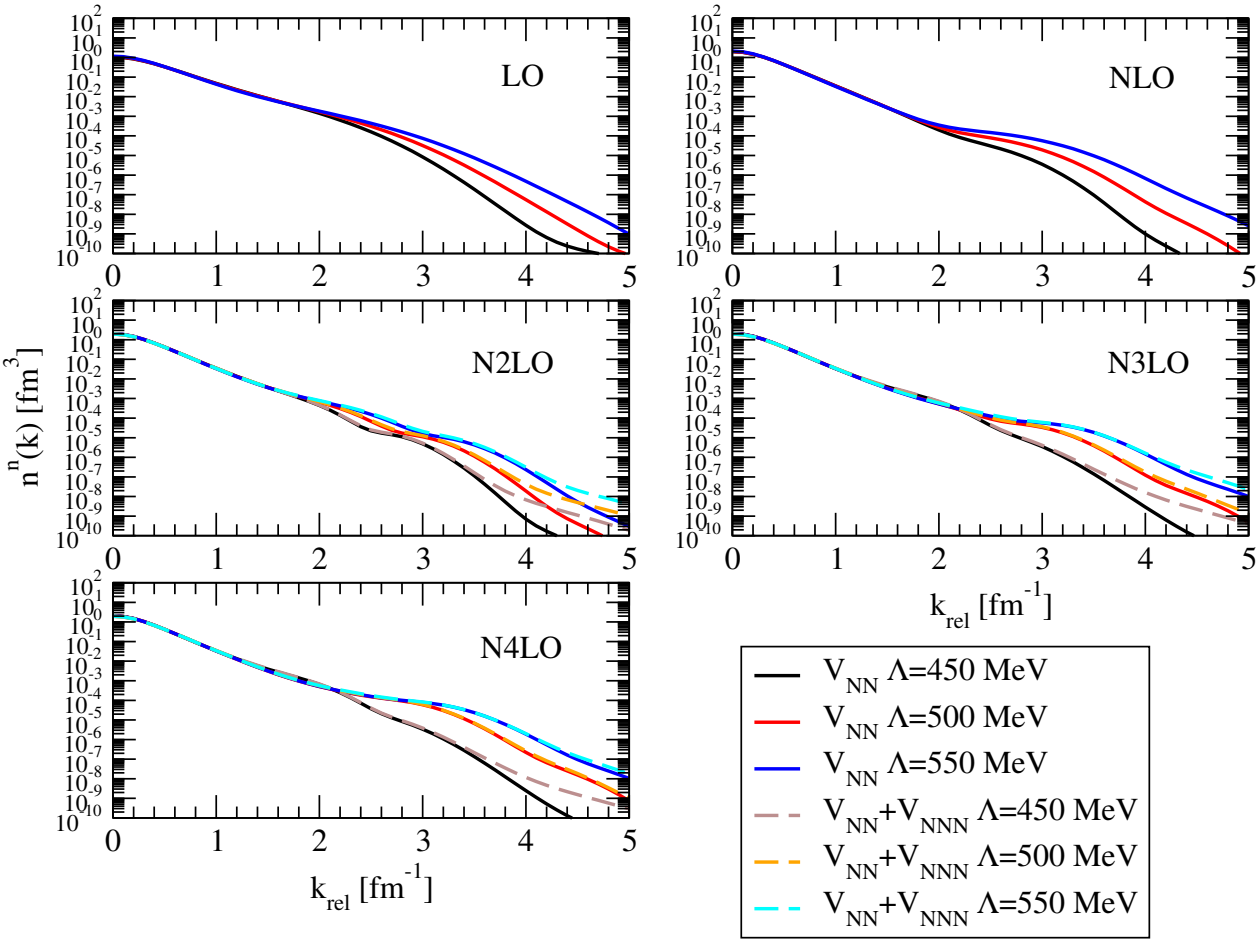

FIG. 6: (Color online) The neutron momentum distributions $n^n(k)$, calculated using only 2N (solid lines) and 2N+3N (dashed lines) chiral interactions, at different chiral order and for three values of the cutoff $\Lambda = 450, 500, 550$ MeV. In all panels, the lines from bottom to top correspond to the lower to higher values of Λ. The LECs of the 3N interaction are those of Table III.

TABLE IV: The integrated p/n probabilities, as defined in Eq. (19), obtained with the various phenomenological potential models, i.e. AV18, CDBonn, AV18/UIX and CDBonn/TM, varying the integration lower bound k_{min}, given in fm^{-1}. We report also the values of Table II of Ref. [26], obtained with the AV18 potential model.

	$P^n(k_{min})$		$P^p(k_{min})$	
	$k_{min} = 0.0$	$k_{min} = 1.5$	$k_{min} = 0.0$	$k_{min} = 1.5$
AV18	0.997	0.068	0.997	0.041
AV18/UIX	0.997	0.077	0.998	0.048
CDBonn	0.998	0.052	0.998	0.031
CDBonn/TM	0.998	0.054	0.999	0.033
Ref. [26]	0.999	0.067	1.000	0.041

functions of heavy-meson masses. On the other hand, the phenomenological AV18 potentials uses a Woods-Saxon function to provide the short-range core. (Heavy mesons, of course, have no place in chiral EFT.) Overall, the chiral predictions fall off at a faster rate as compared to the phenomenological ones. This is to be expected from the "softer" nature of the chiral potentials.

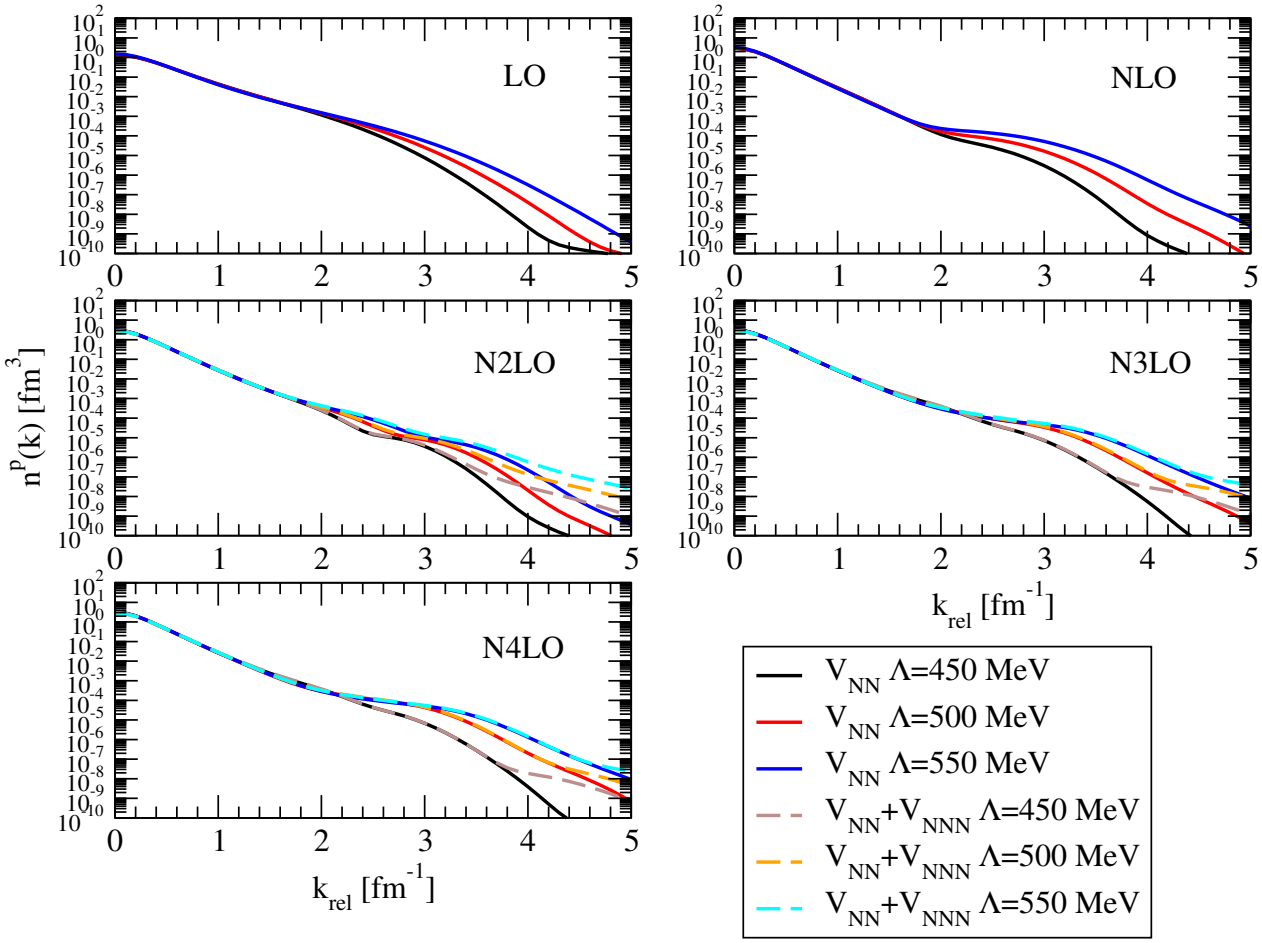

FIG. 7: Same as Fig. 6 but for the proton momentum distributions $n^p(k)$.

C. Two-nucleon momentum distributions and corresponding integrated short-range correlations probabilities

The 2N momentum distribution of the N_1N_2 pair, with $N_1N_2 = np$ or pp, as a function of their relative momentum k_{rel}, is defined as

$$n^{N_1N_2}(k_{rel}, K_{c.m.}) = \int d\hat{\mathbf{k}}_{rel} \int d\hat{\mathbf{k}}_{c.m.} \Psi^\dagger(\mathbf{k}_{rel}, \mathbf{K}_{c.m.}) P_{N_1N_2} \Psi(\mathbf{k}_{rel}, \mathbf{K}_{c.m.}) \ , \tag{21}$$

where $P_{N_1N_2}$ is the projection operator on the N_1N_2 pair. Note that we have introduced the definitions

$$\begin{aligned} \mathbf{k}_{rel} &= -\frac{\sqrt{2}}{2}\mathbf{q}_{p=1} \ , \\ \mathbf{K}_{c.m.} &= -\sqrt{\frac{2}{3}}\mathbf{k}_{p=1} \ , \end{aligned} \tag{22}$$

that is, we have chosen the pair N_1N_2 to contain particles $2, 3$. In the following, we will focus on the so-called back-to-back (BB) 2N momentum distributions, i.e. $n^{N_1N_2}(k_{rel}, K_{c.m.} = 0)$, and on the $K_{c.m.}$-integrated 2N momentum distributions, i.e.

$$n^{N_1N_2}(k_{rel}) = 4\pi \int_0^{K^+_{c.m.}} K^2_{cm}\, dK_{cm} n^{N_1N_2}(k_{rel}, K_{c.m.}) \ . \tag{23}$$

The upper limit of the $K_{c.m.}$-integration restricts the values of $K_{c.m.}$ to a limited range, approximately $K^+_{c.m.} \simeq 1.0{-}1.5$ fm^{-1}. This is because, in the SRC model (as opposed to the mean-field model), one considers highly correlated N_1N_2

TABLE V: Same as Table IV but obtained with chiral potentials, at different chiral orders, for different values of the cutoff Λ, 450, 500 and 550 MeV, also with the inclusion of the 3N force (lines labelled N2LO/N2LO at N2LO, N3LO/N3LO-I and N3LO/N3LO-II at N3LO, N4LO/N4LO-I and N4LO/N4LO-II at N4LO). The labels "I" and "II" refer to the LECs of Table II and III, respectively.

	$P^n(k_{min}=0.0)$			$P^p(k_{min}=0.0)$			$P^n(k_{min}=1.5)$			$P^p(k_{min}=1.5)$		
Model/Λ [MeV]	450	500	550	450	500	550	450	500	550	450	500	550
LO	1.000	1.000	0.999	1.000	0.999	0.999	0.090	0.105	0.113	0.076	0.089	0.095
NLO	0.999	0.999	0.999	0.999	0.999	0.998	0.020	0.025	0.033	0.013	0.016	0.023
N2LO	0.999	0.999	0.999	0.999	0.999	0.999	0.033	0.040	0.046	0.020	0.024	0.027
N2LO/N2LO	0.999	0.999	0.999	0.999	0.999	0.999	0.033	0.040	0.046	0.020	0.024	0.027
N3LO	0.999	0.999	0.999	0.999	0.999	0.999	0.042	0.038	0.041	0.025	0.025	0.026
N3LO/N3LO-I	0.999	0.999	0.999	0.999	0.999	0.999	0.045	0.041	0.045	0.027	0.028	0.030
N3LO/N3LO-II	0.999	0.999	0.999	0.999	0.999	0.999	0.045	0.041	0.045	0.027	0.027	0.029
N4LO	0.999	0.999	0.999	0.999	0.999	0.999	0.041	0.039	0.043	0.024	0.025	0.026
N4LO/N4LO-I	0.999	0.999	0.999	0.999	0.999	0.999	0.043	0.043	0.048	0.026	0.028	0.030
N4LO/N4LO-II	0.999	0.999	0.999	0.999	0.999	0.999	0.043	0.042	0.046	0.026	0.027	0.028

pairs with small center-of-mass momentum [26, 27]. The integrations of Eqs. (21) and (23) have been performed numerically with the Van der Corput sequence [35] and we have verified that our results are stable with the increasing value of Van der Corput points of integrations. Typically, 50 000 points are enough for converged results.

First we calculate the 2N momentum distributions using the AV18 [13] phenomenological potential, with and without the UIX phenomenological 3N force [24], in order to compare with results available in the literature [26–28]. The comparison presented in Fig. 8 shows that we are able to reproduce the results of previous investigations for $n^{N_1N_2}(k_{rel}, K_{c.m.}=0)$, but we have verified a similar degree of agreement also for $n^{N_1N_2}(k_{rel})$. Furthermore, we see that the 3N force contribution is quite small, an observation which will be confirmed throughout the paper.

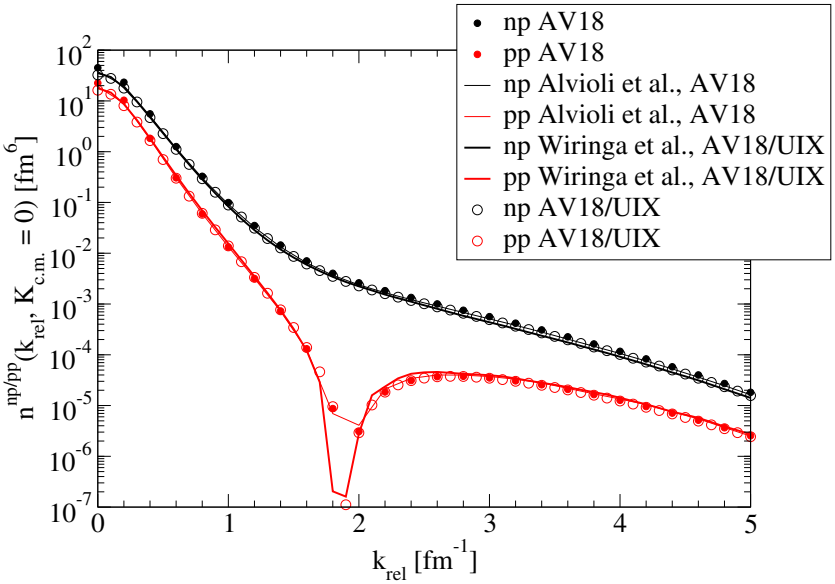

FIG. 8: (Color online) The 2N momentum distributions $n^{np/pp}(k_{rel}, K_{c.m.}=0)$, calculated using the AV18 and the AV18/UIX interaction models. The present results are shown as circles (full for Av18 and enpty for AV18/UIX), while the previous studies of Refs. [26, 27] and Ref. [28] are shown as thin or thick solid lines, respectively. For the *np* case, all the results essentially overlap.

We then move to the $n^{np/pp}(k_{rel})$ 2N momentum distribution as function of $K^+_{c.m.}$ (see Eq. (23)). The results for the AV18/UIX are shown in Fig. 9, from which we can conclude that contributions from $K^+_{c.m.}$ larger than approximately 5 fm^{-1} are not significant. We also note, in passing, that for $K^+_{c.m.}=1.5$ fm^{-1}, the AV18 and AV18/UIX results are very close to each other.

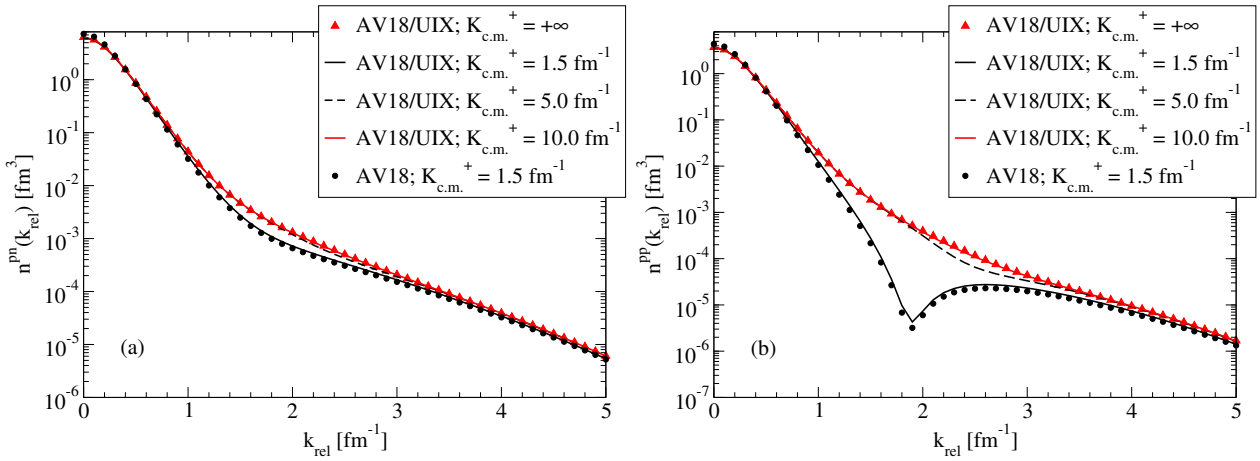

FIG. 9: (Color online) The 2N momentum distributions $n^{np}(k_{rel})$ (panel (a)) and $n^{pp}(k_{rel})$ (panel (b)) as function of $K^{+}_{c.m.}$ (see Eq. (23)), calculated using the AV18/UIX potential. For $K^{+}_{c.m.} = 1.5$ fm^{-1} we show also the results obtained with the AV18 2N only potential. The lines for $K^{+}_{c.m.} = 5$ fm^{-1} and 10 fm^{-1} can barely be distinghuished.

Next we explore the model-dependence of the 2N momentum distributions, by repeating the calculations using the CDBonn potential without or with the TM 3N force. In Figs. 10 and 11 we show the results for the $n^{np/pp}(k_{rel}, K_{c.m.} = 0)$ and for the $n^{np/pp}(k_{rel})$ as function of $K^{+}_{c.m.}$, respectively. The figures reveal that: (i) the results with CDBonn/TM and those with AV18/UIX are substantially different from each other, especially in the high-k_{rel} tails, confirming what we mentioned earlier while recalling the findings of Ref. [12]; (ii) the 3N force contributions are again barely appreciable on the plot (which are on a logarithmic scale); (iii) the $K^{+}_{c.m.}$-dependence in the CDBonn/TM case is very similar to the one seen in the AV18/UIX case.

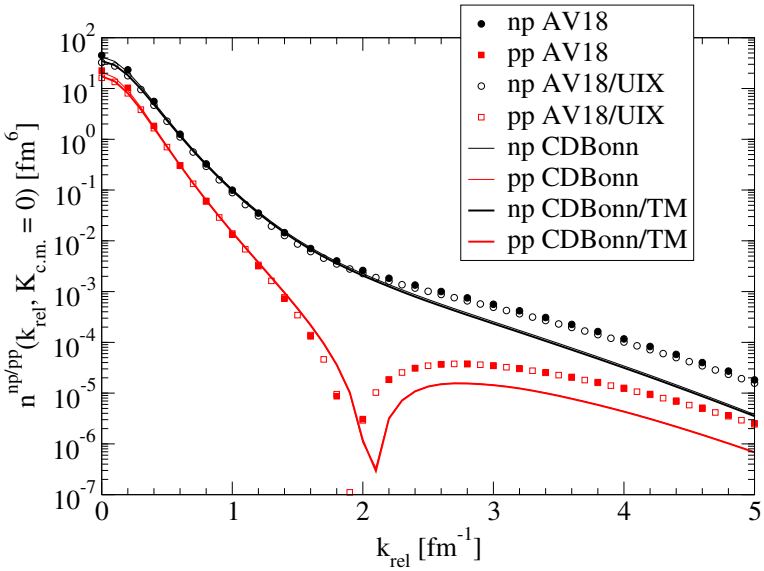

FIG. 10: (Color online) The 2N momentum distributions $n^{np/pp}(k_{rel}, K_{c.m.} = 0)$, calculated using the AV18, AV18/UIX, CDBonn and CDBonn/TM 2N and 3N interaction models. The thin and thik lines are on top of each other and can barely be distinguished.

An important issue in the considerations of SRC is the behavior of $n^{np}(k_{rel})$ in nuclei as compared with the same quantity in the deuteron ($n^{np}_{d}(k_{rel})$). This is because a highly correlated np pair in a nucleus is expected to exhibit a behavior similar to the pair in the deuteron. We proceed to calculate the integrated SRC-probabilities defined as

$$N^{BB}_{N_1N_2} \;=\; 4\pi \int_0^{\infty} n^{N_1N_2}(k_{rel}, K_{c.m.} = 0) k^2_{rel}\, dk_{rel}\ , \tag{24}$$

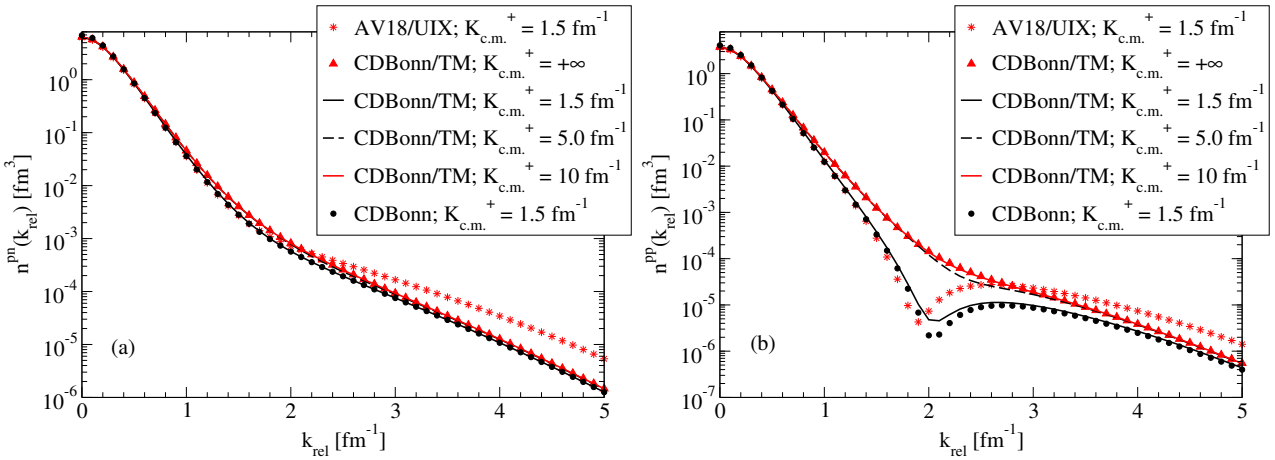

FIG. 11: (Color online) The 2N momentum distributions $n^{np}(k_{rel})$ (panel (a)) and $n^{pp}(k_{rel})$ (panel (b)) as function of $K^+_{c.m.}$ (see Eq. (23)), calculated using the CDBonn/TM potential. For $K^+_{c.m.} = 1.5$ fm^{-1} we show also the results obtained with the CDBonn 2N only potential and the AV18/UIX potential, already presented in Fig. 9. The lines for $K^+_{c.m.} = 5$ fm^{-1} and 10 fm^{-1} can barely be distinghuished.

TABLE VI: The integrated np and pp SRC-probabilities, as defined in Eqs. (24)–(27), obtained with the various potential models, i.e. AV18, CDBonn, AV18/UIX and CDBonn/TM. For the np case, we report in the last two lines labelled AV18 - d and CDBonn - d the deuteron results of Ref. [12].

	$N_1N_2 = np$				$N_1N_2 = pp$			
	N^{BB}	$N^{SRC,BB}$	$N^{SRC}(k_{rel,min})$	N	N^{BB}	$N^{SRC,BB}$	$N^{SRC}(k_{rel,min})$	N
AV18	6.922	0.241	0.093	1.997	2.194	0.009	0.026	0.998
AV18/UIX	5.751	0.210	0.106	1.997	1.897	0.009	0.031	0.999
CDBonn	6.552	0.171	0.060	1.997	2.078	0.005	0.012	0.999
CDBonn/TM	5.931	0.157	0.063	1.998	1.924	0.005	0.014	0.998
AV18 - d			0.042					
CDBonn - d			0.032					

$$N^{SRC,BB}_{N_1N_2} = 4\pi \int_{k_{rel,min}}^{\infty} n^{N_1N_2}(k_{rel}, K_{c.m.} = 0) k^2_{rel}\, dk_{rel} \ , \tag{25}$$

$$N^{SRC}_{N_1N_2}(k_{rel,min}) = 4\pi \int_{k_{rel,min}}^{\infty} n^{N_1N_2}(k_{rel}) k^2_{rel}\, dk_{rel} \ , \tag{26}$$

$$N_{N_1N_2} = 4\pi \int_{0}^{\infty} n^{N_1N_2}(k_{rel}) k^2_{rel}\, dk_{rel} \equiv N^{SRC}_{N_1N_2}(k_{rel,min} = 0) \ , \tag{27}$$

where we have used $k_{rel,min} = 1.5$ fm^{-1}. These equations are the same as in Ref. [26]. For convenience, we will continue to refer to these integrated quantities as probabilities. A more accurate description of, for instance, $N^{BB}_{N_1N_2}$ would be the number of back-to-back N_1N_2 pairs after integration of the pair relative momentum.

The results for the different potential models used so far are shown in Table VI, from which we can conclude that the 3N force contributions are small also for the integrated quantities. However, model-dependence is strong, especially for $N^{SRC,BB}$ and $N^{SRC}(k_{rel,min})$. This large model-dependence might have impact on the extraction of SRC probabilities from $(e, e'p)$ experiments, if not properly taken into account.

We now turn our attention to the 2N momentum distributions obtained with the 2N chiral potentials without or with the 3N forces, obtained as discussed in Sec. III A. We begin with studying the order-by-order pattern, using the $\Lambda = 500$ MeV cutoff as an example. The results obtained with the other values of Λ display a similar behaviour. In panel (a) of Fig. 12 we show the BB np momentum distribution $n^{np}(k_{rel}, K_{c.m.} = 0)$ obtained using only the 2N force at LO, NLO, N2LO, N3LO and N4LO. In panel (b), we present the results for $n^{np}(k_{rel}, K_{c.m.} = 0)$ including the 3N force, with LECs obtained from Table II (model I) and III (model II), respectively. By inspection of the figures, we can conclude that the LO curve has a distinct behavior at small k_{rel} compared with the other curves, which suggests that the asymptotic part of the wave function at LO is significantly different than at the higher orders.

Furthermore, as it will be clearly shown below in Figs. 14 and 15, the 3N force contribution is very small, and therefore the difference between the 3N force models is not visible. Finally, the N3LO and N4LO curves are very similar up to $k_{rel} \simeq 2.2$ fm^{-1}, indicating satisfactory order-by-order convergence at least in the region where the distributions still have non-negligible size. In Fig. 13 we show the corresponding BB *pp* momentum distributions. As we can see, the same remarks apply in the *pp* case as well.

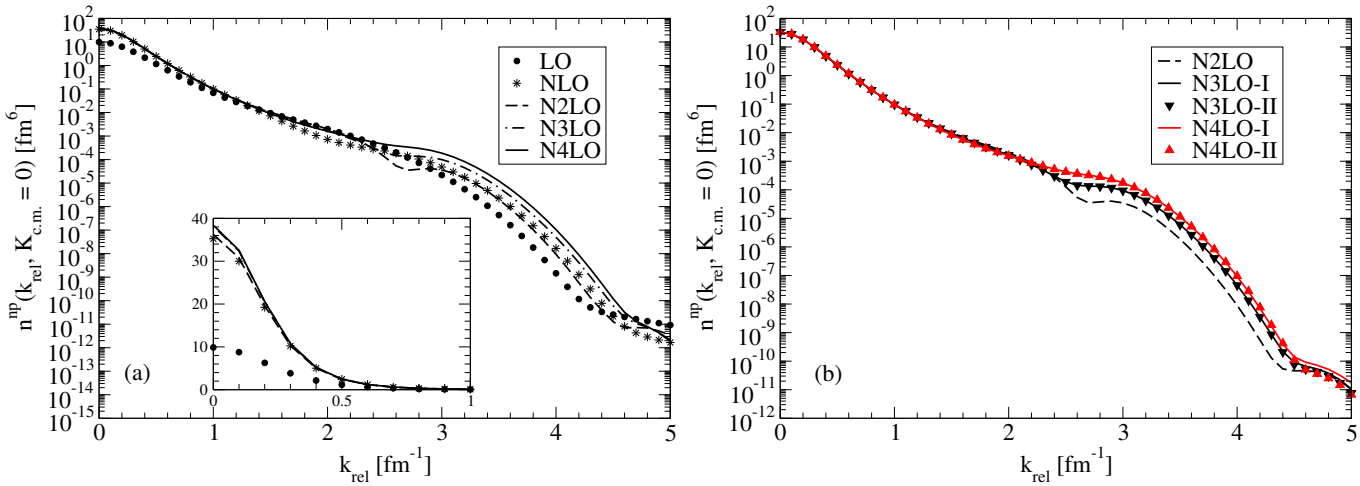

FIG. 12: (Color online) The *np* momentum distributions $n^{np}(k_{rel}, K_{c.m.} = 0)$, calculated using only 2N (panel (a)) and 2N+3N (panel (b)) chiral interactions, with $\Lambda = 500$ MeV. The different chiral orders are labelled as in the text. In the inset of panel (a) we show the small k_{rel} range ($k_{rel} \leq 1$ fm^{-1}) on a linear scale. In panel (b), we indicate with "I" and "II" the results obtained using the LECs of Table II and III, respectively.

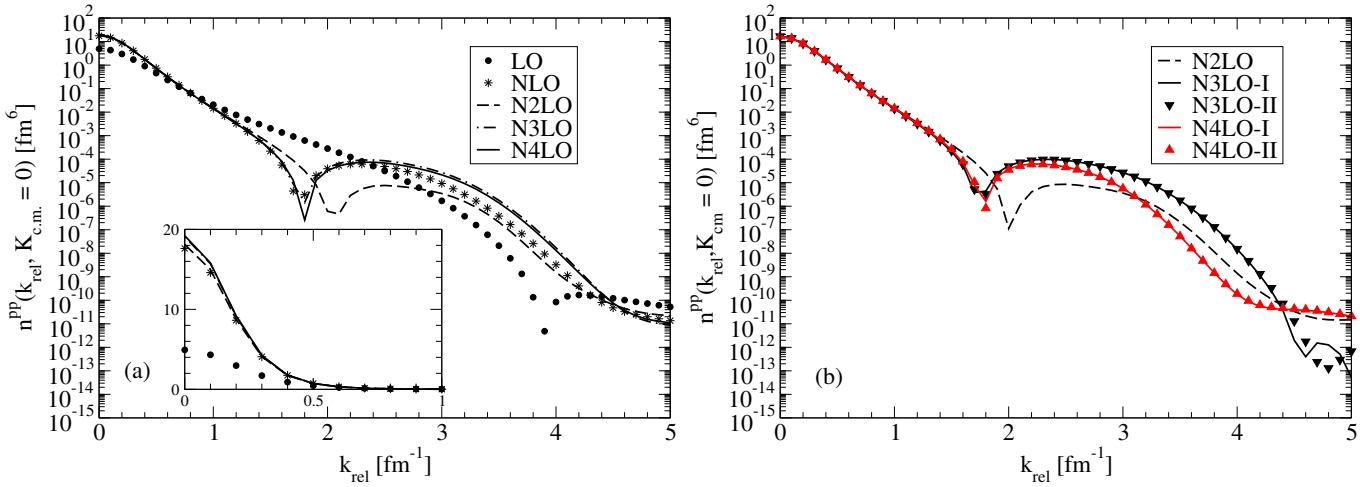

FIG. 13: Same as Fig. 12 but for the *pp* pair.

The BB 2N momentum distributions $n^{np}(k_{rel}, K_{c.m.} = 0)$ and $n^{pp}(k_{rel}, K_{c.m.} = 0)$ calculated with and without 3N interaction, at different chiral order and for different values of the cutoff Λ, are shown in Figs. 14 and 15, respectively. The results for the 2N momentum distributions $n^{np/pp}(k_{rel}, K^{+}_{c.m.})$ for $K^{+}_{c.m.} = +1.5$ fm^{-1} and $K^{+}_{c.m.} = +\infty$ are shown in Figs. 16, 17, 18 and 19. By inspection of all the figures we can conclude that we have essentially no cutoff dependence below $k_{rel} \simeq 2.2 - 2.5$ fm^{-1}, and increasingly strong cutoff dependence above it. Furthermore, the 3N force contributions are visible only for $k_{rel} \geq 3.0 - 3.5$ fm^{-1}. Note, however, that above $k_{rel} \simeq 2.5$ fm^{-1} all momentum distributions are so small that the differences are of no practical relevance, see next.

Calculating the integrated SRCs as defined in Eqs. (24)–(27), we obtain the values displayed in Tables VII and VIII for *np* and *pp* SRCs, respectively. For these "observables", as well, we find that order-by-order convergence is satisfactory and cutoff dependence is weak. This implies that the contributions from the region $k_{rel} \geq 2.2$ fm^{-1} are essentially negligible.

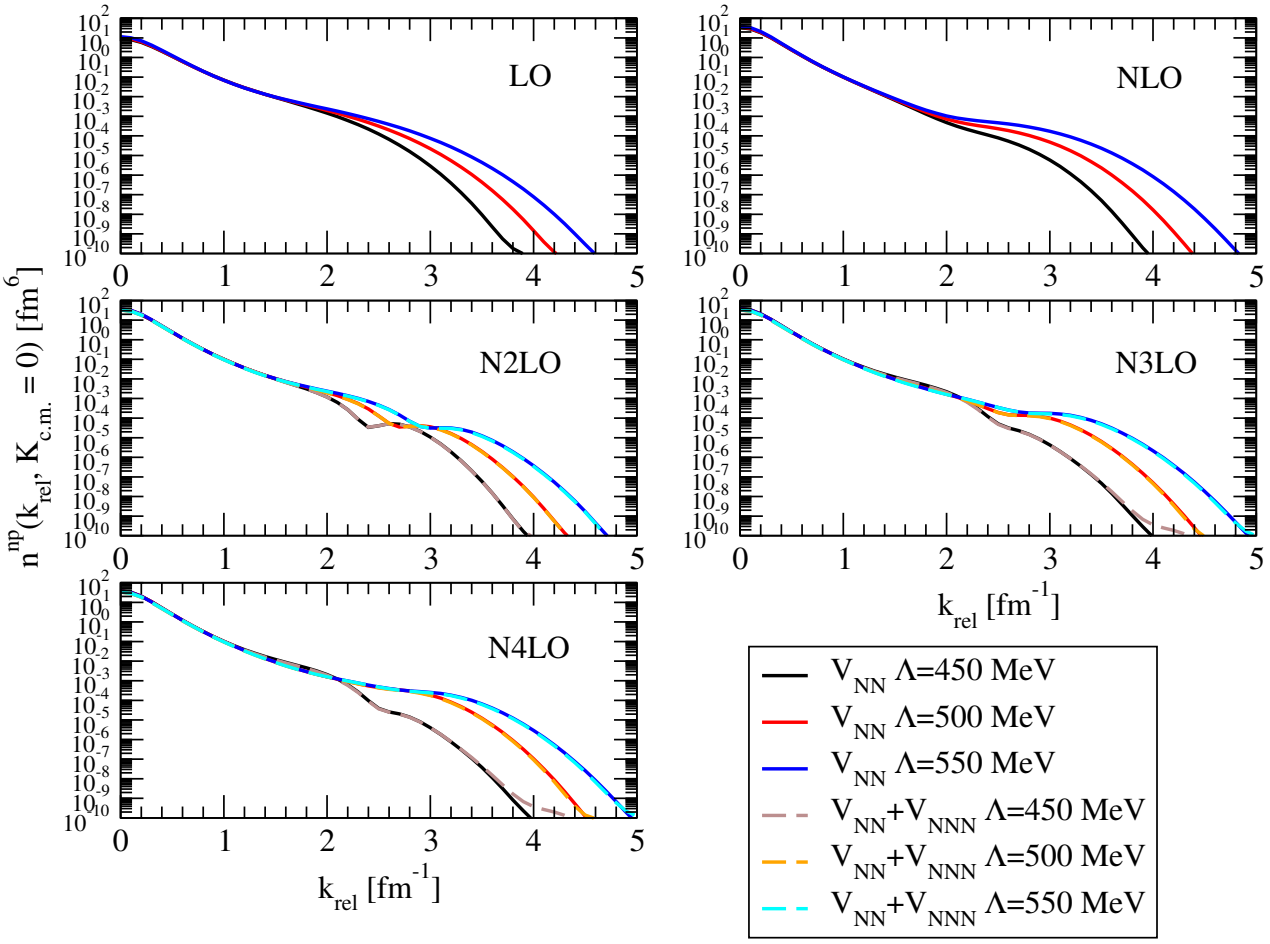

FIG. 14: (Color online) The np momentum distributions $n^{np}(k_{rel}, K_{c.m.} = 0)$, calculated using only 2N (solid lines) and 2N+3N (dashed lines) chiral interactions, at different chiral order and for three values of the cutoff $\Lambda = 450, 500, 550$ MeV. In all panels, the lines from bottom to top correspond to the lower to higher values of Λ. The LECs of the 3N interaction are those of Table III.

Earlier in the paper, we noted that the momentum distributions we calculated with chiral interactions die out at a faster rate than those obtained with phenomenological potentials. In Sect. III B, we pointed out that such feature may be expected given the softer nature of chiral forces. While this is a correct observation within the spectrum of interactions considered here, it is important to note that the chiral nature of an interaction does not necessarily bring additional softness. To support this statement, we refer to Ref. [43], where predictions for 1N and 2N momentum distributions in $A \leq 16$ are shown. In that work it is concluded that, when *local* chiral interactions are employed, the resulting momentum distributions are *consistent* with those obtained from local phenomenological potentials. In fact, the local 2N chiral interactions (at N2LO) applied in Ref. [43] and developed in Refs. [44, 45] predict a D-state probability for the deuteron ranging between 5.5 and 6.1%, values which are typical for the "hardest" local potentials.

Therefore, once again, the local *vs.* non-local nature of the 2N force (by far the largest contribution to the 1N and 2N momentum distributions, as we have observed on several occasions), is a major factor in determining the theoretical momentum distributions in nuclei and, particularly, their short-range part.

IV. CONCLUSIONS AND OUTLOOK

We have presented predictions for 1N and 2N momentum distributions in the deuteron and in ^{3}He. We have employed state-of-the-art chiral 2N potentials (with or without the leading chiral 3N force) and also, for the purpose of comparison and validation of our tools, older potentials plus 3N force, either fully phenomenological or based on meson theory. A main motivation was to explore the short-range few-nucleon dynamics as predicted by these diverse interactions. One of our findings is that, regardless the 2N force model, the contribution from 3N forces is always

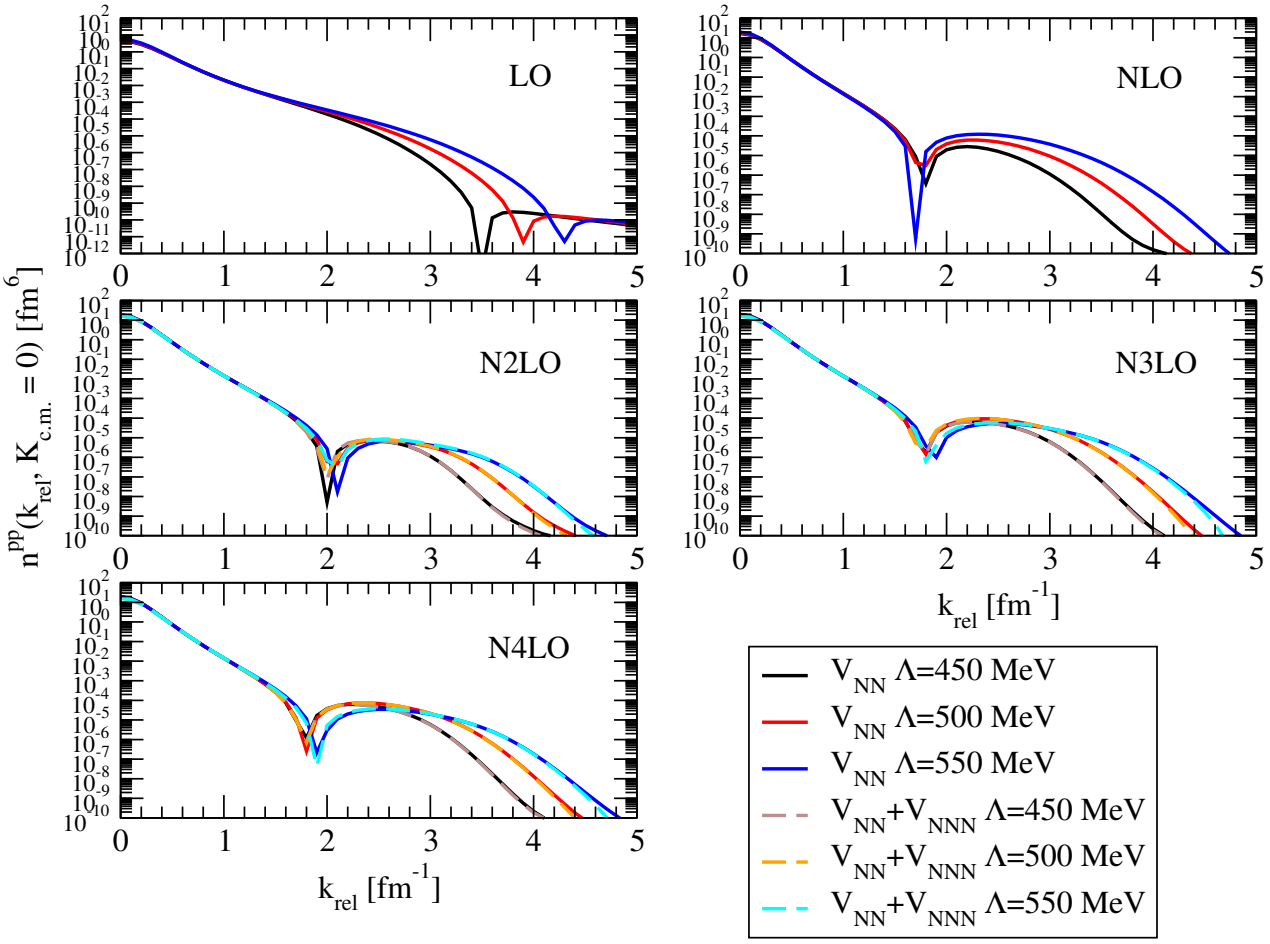

FIG. 15: Same as Fig. 14 but for the *pp* pair.

very weak.

We have also quantified and pointed out, as appropriate, any significant model-dependence, especially in the high-momentum tails of the momentum distributions. Model dependence is large with both phenomenological and chiral potentials. We have explored cutoff dependence and found that it can be significant. This is the case, though, in the region where the momentum becomes larger than the cutoff values themselves.

Although potentials based on chiral EFT may be expected to produce weaker SRC than purely phenomenological or meson-exchange ones, on several occasions the discussion of model dependence led back to considerations of locality *vs.* non-locality of the underlying 2N force, rather than "chiral" *vs.* "non-chiral". We find this to be an important issue, extensively debated in the literature of the 1990's [19–21] and now re-emerging in the light of new stimulating discussions.

The 2N potentials considered here have an established success record with low-energy predictions, such as the structure of light and medium-mass nuclei as well as the properties of nuclear matter. But, as shown above, they differ considerably in their high-momentum components. Note that there is no physical reason why the off-shell behavior of, say, AV18, should be preferable as compared to other potentials. In fact, on fundamental grounds off-shell behavior is not observable. To stress this point even more: 2N potentials which are known as V_{low-k} [46] are typically cut off between 1.5 and 2 fm^{-1} and, thus, produce essentially zero SRC. However, these low-momentum interactions are highly successful in *ab initio* nuclear structure calculations and, thus, are valid 2N potentials. On the other hand, high momentum transfer reactions are easier to analyze using one-body currents of the impulse approximation, suitable with harder 2N potentials, whereas the use of low-momentum potentials complicates the currents necessary to describe high momentum transfer experiments [47].

Although the chiral potentials considered here are not SRG-evolved interactions, they are non-local and rather soft, and thus the above arguments should apply to them as well. It will be interesting to explore the feasibility of describing "hard scattering" data (in the form of cross section ratios [8, 48, 49]) with these softer, non-local potentials.

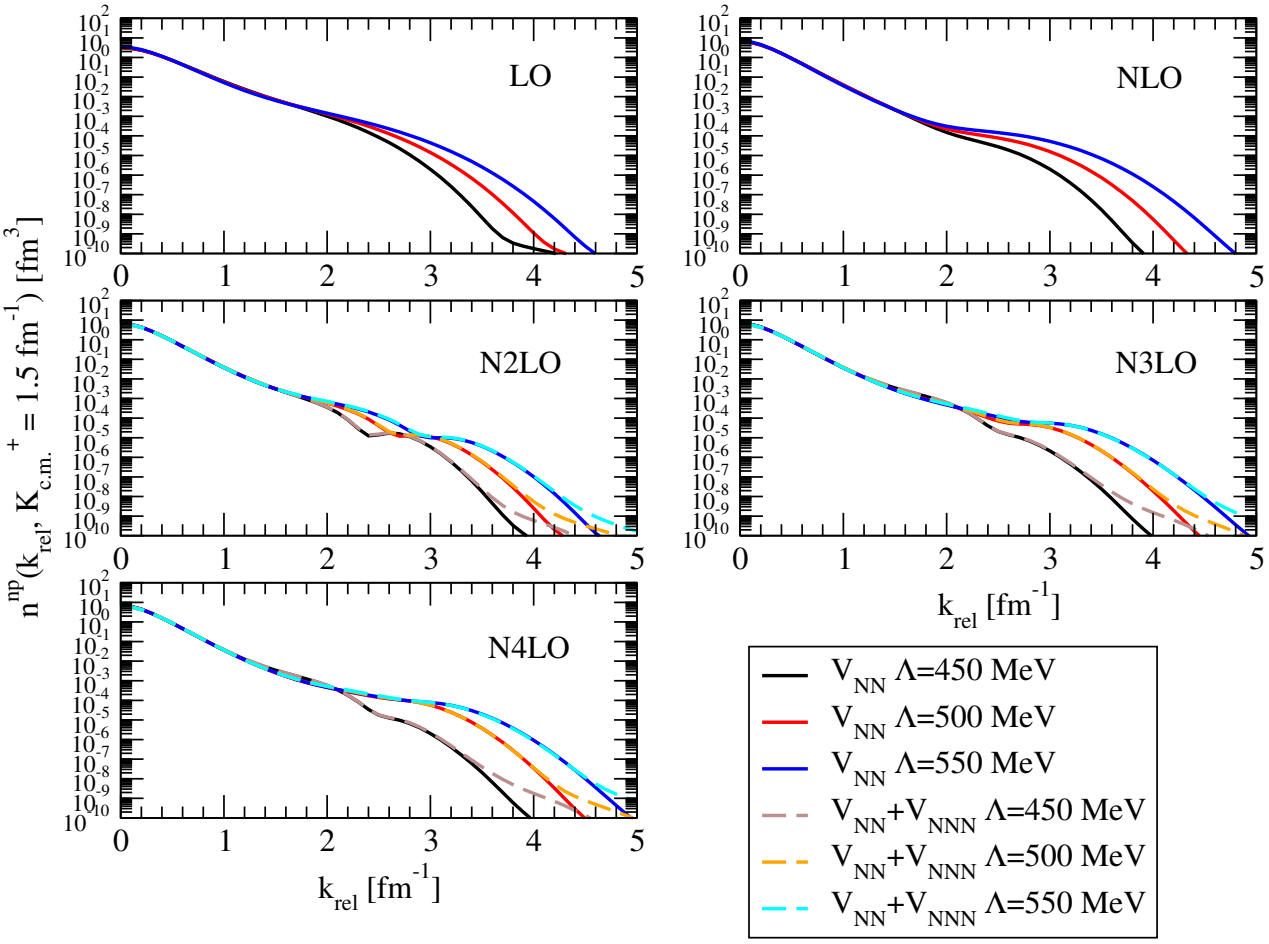

FIG. 16: (Color online) The 2N momentum distributions $n^{np}(k_{rel}, K^{+}_{c.m.})$ for $K^{+}_{c.m.} = +1.5$ fm^{-1}, calculated using only 2N (solid lines) and 2N+3N (dashed lines) chiral interactions, at different chiral order and for three values of the cutoff $\Lambda = 450, 500, 550$ MeV. In all panels, the lines from bottom to top correspond to the lower to higher values of Λ. The LECs of the 3N interaction are those of Table III.

We are presently extending our study of momentum distributions to include triton and ^{4}He.

Acknowledgments

The work of F.S. and R.M. was supported by the U.S. Department of Energy, Office of Science, Office of Basic Energy Sciences, under Award Number DE-FG02-03ER41270. Computational resources provided by the INFN-Pisa Computer Center are gratefully acknowledged.

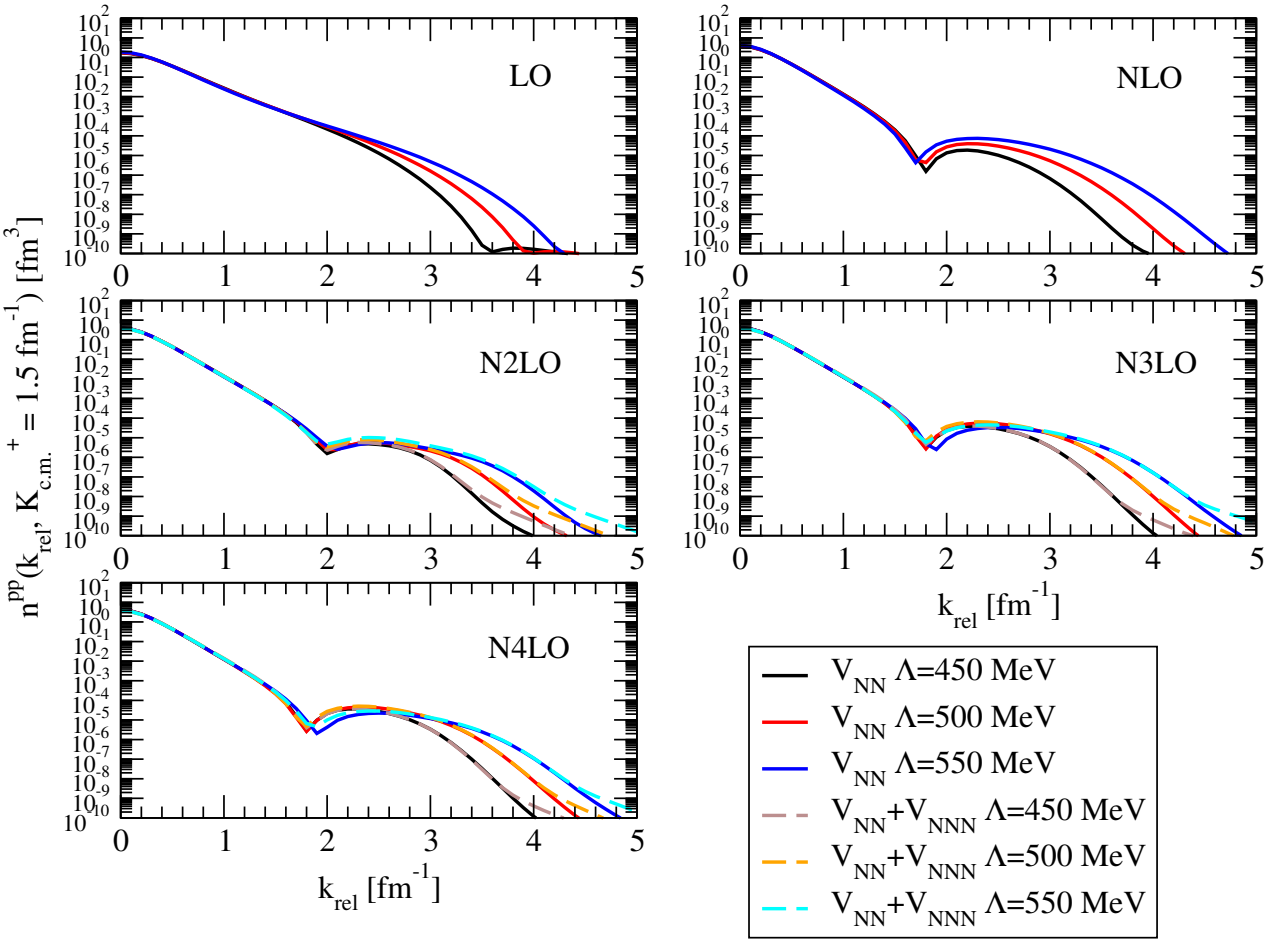

FIG. 17: Same as Fig. 16 but for the *pp* pair.

TABLE VII: The integrated *np* SRC-probabilities, as defined in Eqs. (24)–(27), obtained with chiral potentials, at different chiral orders, for different values of the cutoff Λ, 450, 500 and 550 MeV, also with the inclusion of the 3N force (lines labelled N2LO/N2LO at N2LO, N3LO/N3LO-I and N3LO/N3LO-I at N3LO, N4LO/N4LO-I and N4LO/N4LO-I at N4LO). The labels "I" and "II" refer to the LECs of Table II or III, respectively.

	N^{BB}			$N^{SRC,BB}$			$N^{SRC}(k_{rel,min})$			N		
Model/Λ [MeV]	450	500	550	450	500	550	450	500	550	450	500	550
LO	2.731	2.829	3.051	0.094	0.120	0.144	0.089	0.112	0.126	1.999	1.999	1.998
NLO	5.896	6.054	6.458	0.047	0.066	0.096	0.016	0.024	0.037	1.998	1.998	1.997
N2LO	5.977	6.127	6.236	0.087	0.118	0.141	0.029	0.038	0.045	1.998	1.997	1.997
N2LO/N2LO	5.844	5.831	5.827	0.086	0.114	0.135	0.030	0.040	0.050	1.998	1.998	1.998
N3LO	6.443	6.314	6.317	0.131	0.112	0.122	0.039	0.039	0.044	1.997	1.997	1.997
N3LO/N3LO-I	5.823	5.884	5.907	0.121	0.107	0.117	0.042	0.043	0.051	1.998	1.998	1.998
N3LO/N3LO-II	5.817	5.865	5.890	0.121	0.107	0.117	0.042	0.043	0.050	1.998	1.998	1.998
N4LO	6.360	6.345	6.266	0.125	0.119	0.129	0.038	0.042	0.047	1.997	1.997	1.998
N4LO/N4LO-I	5.823	5.911	5.915	0.116	0.114	0.125	0.041	0.047	0.054	1.998	1.998	1.998
N4LO/N4LO-II	5.809	5.868	5.857	0.116	0.113	0.123	0.040	0.045	0.051	1.998	1.998	1.998

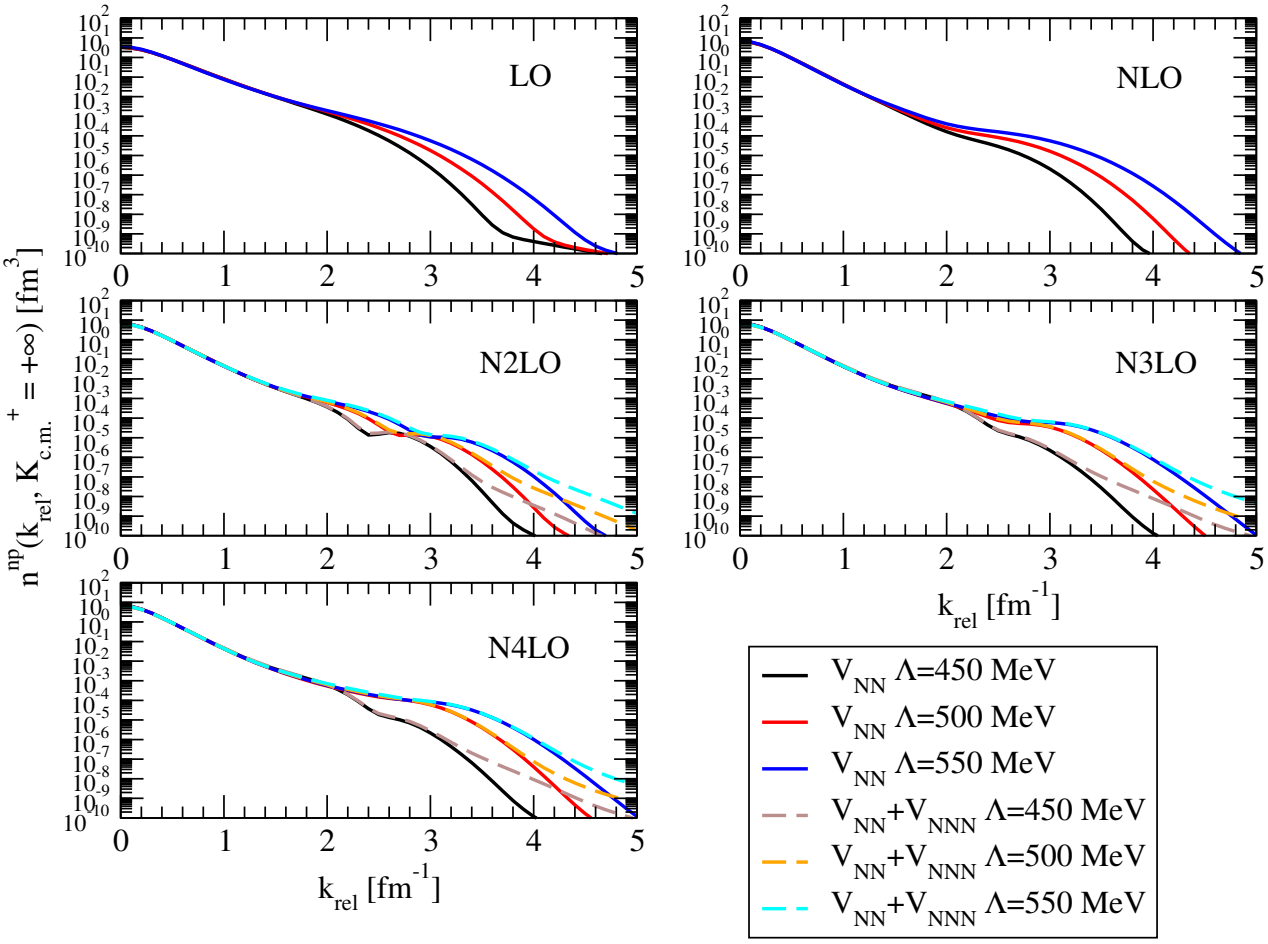

FIG. 18: Same as Fig. 16 but for $K^{+}_{c.m.} = +\infty$.

TABLE VIII: Same as Table VII but for the *pp* pair.

	N^{BB}			$N^{SRC,BB}$			$N^{SRC}(k_{rel,min})$			N		
Model/Λ [MeV]	450	500	550	450	500	550	450	500	550	450	500	550
LO	1.049	1.087	1.165	0.016	0.020	0.023	0.030	0.040	0.045	0.999	0.999	0.999
NLO	1.976	2.014	2.109	0.002	0.004	0.009	0.002	0.004	0.010	0.999	0.999	0.998
N2LO	1.975	2.009	2.036	0.002	0.002	0.003	0.003	0.004	0.005	0.998	0.998	0.998
N2LO/N2LO	1.943	1.935	1.932	0.002	0.002	0.002	0.003	0.004	0.006	0.999	0.998	0.998
N3LO	2.083	2.061	2.060	0.004	0.007	0.006	0.003	0.007	0.009	0.998	0.998	0.998
N3LO/N3LO-I	1.928	1.952	1.958	0.004	0.007	0.006	0.004	0.009	0.011	0.998	0.999	0.999
N3LO/N3LO-II	1.927	1.948	1.953	0.004	0.007	0.006	0.004	0.008	0.011	0.998	0.999	0.999
N4LO	2.064	2.070	2.048	0.004	0.005	0.004	0.004	0.008	0.009	0.998	0.998	0.998
N4LO/N4LO-I	1.929	1.960	1.962	0.004	0.006	0.004	0.004	0.009	0.012	0.998	0.999	0.999
N4LO/N4LO-II	1.926	1.949	1.945	0.004	0.005	0.004	0.004	0.009	0.010	0.998	0.999	0.999

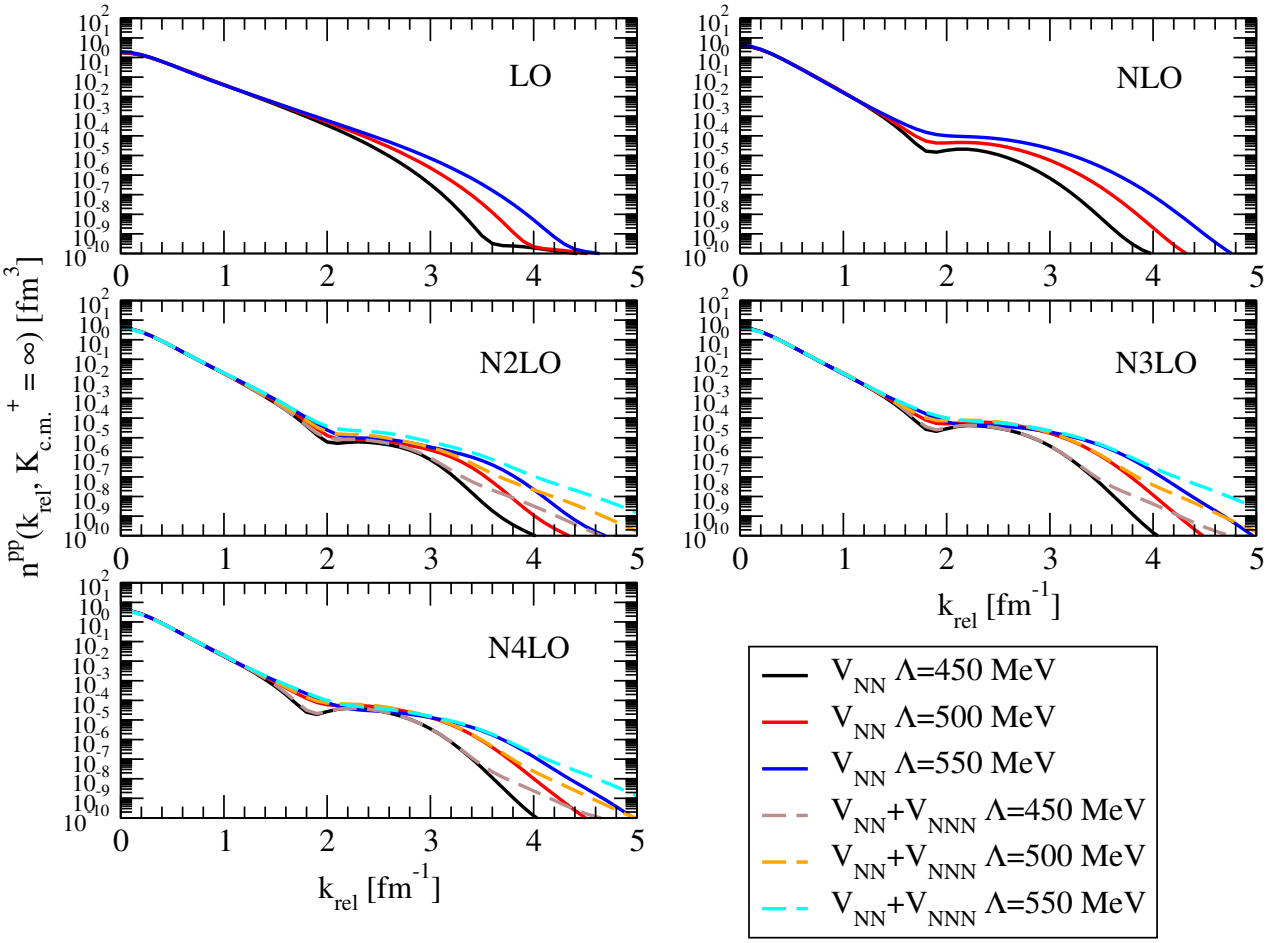

FIG. 19: Same as Fig. 18 but for the *pp* pair.

[1] K.S. Egiyan *et al.*, Phys. Rev. Lett. **96**, 082501 (2006), and references therein.
[2] K.S. Egiyan *et al.*, CLAS-NOTE 2005-004, 2005, www1.jlab.org/ul/Physics/Hall-B/clas.
[3] K.S. Egiyan et al., Phys. Rev. C **68**, 014313 (2003).
[4] Michael McGauley and Misak M. Sargsian, arXiv:1102.3973v3 (2012).
[5] E. Piasetzky *et al.*, Phys. Rev. Lett. **97**, 162504 (2006).
[6] F. Sammarruca, Phys. Rev. C **90** , 064312 (2014); and references therein.
[7] A. Tang *et al.*, Phys. Rev. Lett. **90**, 042301 (2003).
[8] I. Korover *et al.* (Jefferson Lab Hall A Collaboration), Phys. Rev. Lett. **113**, 022501 (2014).
[9] R. Shneor *et al.* (Jefferson Lab Hall A Collaboration), Phys. Rev. Lett. **99**, 072501 (2007).
[10] R. Subedi *et al.*, Science **320**, 1476 (2008).
[11] H. Baghdasaryan *et al.* (CLAS Collaboration), Phys. Rev. Lett. **105**, 222501 (2010).
[12] F. Sammarruca, Phys. Rev. C **92**, 044003 (2015).
[13] R.B. Wiringa, V.G.J. Stoks, and R. Schiavilla, Phys. Rev. C **51**, 38 (1995).
[14] V.G.J. Stoks, R.A.M. Klomp, C.P.F. Terheggen, and J.J. de Swart, Phys. Rev. C **49**, 2950 (1994).
[15] R. Machleidt, Phys. Rev. C **63**, 024001 (2001).
[16] D.R. Entem and R. Machleidt, Phys. Rev. C **68**, 041001, (2003).
[17] E. Marji, A. Canul, Q. MacPherson, R. Winzer, Ch. Zeoli, D.R. Entem, and R. Machleidt, Phys. Rev. C **88**, 054002 (2013).
[18] R. Machleidt and D.R. Entem, Phys. Rep. **503**, 1 (2011).
[19] R. Machleidt, F. Sammarruca, and Y. Song, Phys. Rev. C **53**, 1483 (1996).
[20] A. Polls, H. Müther, R. Machleidt, and M. Hjorth-Jensen, Phys. Lett. B **432**, 1 (1998).
[21] H. Müther and A.Polls, Phys. Rev. C **61**, 014304 (1999).
[22] D.R. Entem, R. Machleidt, and Y. Nosyk, Phys. Rev. C **96**, 024004 (2017).
[23] M. Hoferichter, J. Ruiz, de Elvira, B. Kubis, and U.-G. Meissner, Phys. Rev. Lett. **115**, 192301 (2015); Phys. Rep. **625**, 1 (2016).
[24] B.S. Pudliner, V.R. Pandharipande, J. Carlson, and R.B. Wiringa, Phys. Rev. Lett. **74**, 4396 (1995).
[25] S.A. Coon and H.K. Han, Few-Body Systems **30**, 131 (2001).
[26] M. Alvioli, C. Ciofi degli Atti, L.P. Kaptari, C.B. Mezzetti, and H. Morita, Phys. Rev. C **87**, 034603 (2013).
[27] M. Alvioli, C. Ciofi degli Atti, and H. Morita, Phys. Rev. C **94**, 044309 (2016).
[28] R.B. Wiringa, R. Schiavilla, S. Pieper, and J. Carlson, Phys. Rev. C **89**, 024305 (2014); R.B. Wiringa, `https://www.phy.anl.gov/theory/research/momenta2/`
[29] M. Viviani *et al.*, Few-Body Syst. **39**, 159 (2006)
[30] A. Kievsky *et al.*, J. Phys. G **35**, 063101 (2008)
[31] L.E. Marcucci, A. Kievsky, S. Rosati, R. Schiavilla, and M. Viviani, Phys. Rev. Lett. **108**, 052502, (2012); Erratum: Phys. Rev. Lett. **121**, 049901 (2018).
[32] F. Sammarruca, L.E. Marcucci, L. Coraggio, J.W. Holt, N. Itaco, and R. Machleidt, arXiv:1807.06640.
[33] H. Krebs, A. Gasparyan, and E. Epelbaum, Phys. Rev. C **85**, 054006 (2012).
[34] E. Epelbaum, H. Krebs, and Ulf-G. Meissner, Eur. Phys. J. **A51**, 53 (2015).
[35] J.G. Van der Corput, Akademie van Wetenschappen **38**, 813 (1935).
[36] L. L. Frankfurt, M.I. Strikman, D.B. Day, and M. Sargsyan, Phys. Rev. C **48**, 2451 (1993).
[37] C. Ciofi degli Atti and S. Simula, Phys. Rev. C **53**, 1689 (1996).
[38] A. Nogga *et al.*, Phys. Rev. C **67**, 034004 (2003).
[39] V. Bernard, E. Epelbaum, H. Krebs, and Ulf-G. Meissner, Phys. Rev. C **77**, 064004 (2008); Phys. Rev. C **84**, 054001 (2011).
[40] H. Krebs, A. Gasparyan, and E. Epelbaum, Phys. Rev. C **85**, 054006 (2012); Phys. Rev. C **87**, 054007 (2013).
[41] L. Girlanda, A. Kievsky, and M. Viviani, Phys. Rev. C **84**, 014001 (2011).
[42] E. Piasetzky, O. Hen, and L.B. Weinstein, AIP Conf. Proc. 1560, 355 (2013).
[43] D. Lonardoni, S. Gandolfi, X.B. Wang, and J. Carlson, arXiv:1804.08027.
[44] A. Gezerlis, I. Tews, E. Epelbaum, S. Gandolfi, K. Hebeler, A. Nogga, and A. Schwenk, Phys. Rev. Lett **111**, 032501 (2013).
[45] A. Gezerlis, I. Tews, E. Epelbaum, M. Freunek, S. Gandolfi, K. Hebeler, A. Nogga, and A. Schwenk, Phys. Rev. C **90**, 054323 (2014).
[46] S.K. Bogner, T.T.S. Kuo, and A. Schwenk, Phys. Rep. **386**, 1 (2003).
[47] Or Hen, Gerald A. Miller, Eli Piasetzky, and Lawrence B. Weinstein, Rev. Mod. Phys. **89**, 045002 (2017).
[48] R. Subedi *et al.*, Science **320**, 1476 (2008).
[49] O. Hen *et al.*, Science **346**, 614 (2014).